Remote Sensing of Environment 209 (2018) 343–362

Contents lists available at ScienceDirect

Remote Sensing of Environment

journal homepage: www.elsevier.com/locate/rse

Evaluation of summer passive microwave sea ice concentrations in the Chukchi Sea based on KOMPSAT-5 SAR and numerical weather prediction data

Hyangsun Han, Hyun-cheol Kim*

Unit of Arctic Sea-Ice Prediction, Korea Polar Research Institute, Incheon, Republic of Korea

ARTICLE INFO

Keywords:
Sea ice concentration
Sea ice algorithm
Passive microwave sensor
KOMPSAT-5
Synthetic aperture radar
Numerical weather prediction
Chukchi Sea

ABSTRACT

Satellite passive microwave (PM) sensors have observed sea ice in Polar Regions and provided sea ice concentration (SIC) data since the 1970s. SIC has been used as a primary data source for climate change prediction and ship navigation. However, the accuracy of PM SIC is typically low and biased in summer. To provide more accurate information for climatic research and ship navigation, it is necessary to evaluate quantitatively the accuracy of PM SIC and to account for its errors. In this research, we evaluated the SIC data derived from PM measurements using four representative sea ice algorithms: NASA Team (NT), Bootstrap (BT), Ocean and Sea Ice Satellite Application Facility (OSISAF) hybrid, and Arctic Radiation and Turbulence Interaction STudy (ARTIST) Sea Ice (ASI). Analyses were performed for the Chukchi Sea in summer using KOrean Multi-Purpose SATellite-5 (KOMPSAT-5) Enhanced Wide-swath synthetic aperture radar (SAR) images. Ice/water maps were generated by binary classification of texture features in the SAR images based on Random Forest, a rule-based machine learning approach. SIC values estimated from the sea ice algorithms showed good correlation with those calculated from the KOMPSAT-5 ice/water maps, but the root mean square error was larger than 10%. SIC values estimated from the algorithms showed different error trends according to the KOMPSAT-5 SIC range. All algorithms overestimated SIC values in open drift ice zones (KOMPSAT-5 SICs ranged from 0% to 15%). In marginal ice zones (SICs ranged from 15% to 80%), the OSISAF SIC values were the least biased compared to those from KOMPSAT-5. The NT algorithm largely underestimated SIC values in marginal ice zones, while the BT and ASI algorithms overestimated them considerably. All algorithms, except for BT, underestimated SIC in consolidated pack ice zones (SICs ranged from 80% to 100%). By analyzing the correlations of biases of SIC from the algorithms with the numerical weather prediction (NWP) data from the European Reanalysis Agency Interim reanalysis, it was found that the overestimation of NT and ASI SICs was largely influenced by atmospheric water vapor content, while the underestimation of NT and OSISAF SICs was owing to ice surface melting. The overestimation of BT SICs was not significantly correlated with the NWP data. The underestimated SIC from the BT and ASI algorithms for high SIC regions might be compensated by the atmospheric water vapor content. The differences in SIC values estimated from each algorithm were due to different sensitivities to atmospheric water vapor content in the regions with KOMPSAT-5 SIC lower than 40% and to ice surface melting in the regions with higher KOMPSAT-5 SIC.

1. Introduction

Arctic sea ice is an important factor in the global climate system. The rapid decrease in the Arctic sea ice extent is a significant indicator of global warming (Johannessen et al., 2004; Screen and Simmonds, 2010; Kay et al., 2011; Mahlstein and Knutti, 2012; Stroeve et al., 2012). Moreover, the change in Arctic sea ice extent influences biological habitats and human activities in the region (Arrigo et al., 2008; Grebmeier et al., 2010; Ho, 2010; Kovacs et al., 2011; Inoue et al., 2015). As the most rapid change in Arctic sea ice extent typically occurs in summer and autumn (Holland et al., 2006; Comiso et al., 2008; Zhang et al., 2008; Overland and Wang, 2013), it is vital to observe sea ice during these seasons. Since the 1970s, passive microwave (PM) sensors have made observations of Arctic and Antarctic sea ice distributions based on the distinct microwave radiation properties between sea ice and open water. These observations have provided daily sea ice concentration (SIC) values, which are defined as the ratio of sea ice-covered area to the total area under consideration, with a grid size

* Corresponding author.
E-mail address: kimhc@kopri.re.kr (H.-c. Kim).

https://doi.org/10.1016/j.rse.2018.02.058
Received 31 July 2017; Received in revised form 5 January 2018; Accepted 22 February 2018
Available online 19 March 2018

of 3–25 km (Steffen and Schweiger, 1991; Comiso et al., 1997; Markus and Cavalieri, 2000; Comiso et al., 2003; Andersen et al., 2007; Spreen et al., 2008). SICs derived from PM measurements have been used for the estimation of sea ice area and extent (Cavalieri and Parkinson, 2012; Ivanova et al., 2014), and currently serve as the primary data source for research on global climate change (Vinnikov et al., 1999; Vihma, 2014; Swart et al., 2015) and ship navigation (Khon et al., 2010; Y. Kim et al., 2014).

The Special Sensor Microwave Imager/Sounder (SSMIS) onboard the Defense Meteorological Satellite Program (DMSP) satellites (Kunkee et al., 2008), and the Advanced Microwave Scanning Radiometer-2 (AMSR2) onboard the Global Change Observation Mission-Water (GCOM-W) satellite (Imaoka et al., 2010; Okuyama and Imaoka, 2015) are representative PM sensors that have been observing sea ice since 2008 and 2012, respectively. The SSMIS continues the missions of the Special Sensor Microwave/Imager (SSM/I), while the AMSR2 is a replacement and successor of the Advanced Microwave Scanning Radiometer (AMSR) and the Advanced Microwave Scanning Radiometer-Earth Observing System (AMSR-E), respectively. There are many algorithms for the estimation of SIC from PM measurements. Among them, the NASA Team (NT) algorithm (Cavalieri et al., 1984) and a hybrid algorithm (Breivik et al., 2001; Tonboe et al., 2016) based on the Bristol (Smith, 1996) and Bootstrap (BT) frequency mode (Comiso, 1986; Comiso et al., 1997) have operationally been used for the estimation of SIC from SSMIS measurements at the National Snow and Ice Data Center (NSIDC) and the European Organisation for the Exploitation of Meteorological Satellites (EUMESAT)'s Ocean and Sea Ice Satellite Application Facility (OSISAF), respectively. For operational estimates of SIC using AMSR2 measurements, the Japan Aerospace Exploration Agency (JAXA) uses the BT algorithm (Comiso, 1986) as a standard algorithm. The Institute of Environmental Physics (IUP) at the University of Bremen and the Integrated Climate Data Center (ICDC) at the University of Hamburg have provided operational AMSR2 SIC products using the Arctic Radiation and Turbulence Interaction STudy (ARTIST) Sea Ice (ASI) algorithm (Spreen et al., 2008), which was developed based on high frequency channels of PM sensors. The IUP has also provided BT SIC products based on AMSR2 measurements.

Many studies have evaluated the SICs estimated from such operational sea ice algorithms using satellite optical and synthetic aperture radar (SAR) images. The NT SICs have been typically underestimated during the Arctic summer (Lubin et al., 1997; Belchansky and Douglas, 2002; Markus and Dokken, 2002; Meier, 2005). Although BT SIC values are typically higher than NT SICs, they have generally been underestimated in the summer season compared to optical and SAR image-derived SIC values (Belchansky and Douglas, 2002; Meier, 2005). The OSISAF algorithm typically retrieves erroneous SIC values in summer (Tonboe et al., 2016). The performance of SIC retrievals from the ASI algorithm was evaluated as being similar to that of the BT algorithm (Spreen et al., 2008), showing a negative bias in the sea ice melting season (Ivanova et al., 2015; Zhao et al., 2015). Based on previous studies, most sea ice algorithms used for SIC estimation from PM measurements show significant inaccuracies in the Arctic summer. As varied channels with different footprints and sensitivities to atmospheric water content and surface emissivity are used, the algorithms can show different SIC estimation performances (Ivanova et al., 2015).

Medium-low resolution satellite optical images such as the Moderate Resolution Imaging Spectroradiometer (MODIS) and the Advanced Very High-Resolution Radiometer (AVHRR) data have been widely used to evaluate sea ice algorithms owing to their wide coverage and low cost (Belchansky and Douglas, 2002; Meier, 2005; Cavalieri et al., 2006; Heinrichs et al., 2006; Cavalieri et al., 2010). However, the optical images are limited by weather conditions and sun altitude; thus, it is very difficult to ensure a high success rate of obtaining cloud-free images with high sun elevation. Moreover, they have a spatial resolution of 500–1000 m in visible wavelengths, which cannot detect sea ice in small sizes, especially during the peak melting summer season when ice floes are fragmented. SAR, an active remote sensing system using microwave, can observe sea ice regardless of weather conditions and sun altitude (Zakhvatkina et al., 2013; Dabboor and Geldsetzer, 2014; Leigh et al., 2014; Han et al., 2016; Han et al., 2017). Current SAR satellites can observe wide areas of a few square kilometers with high spatial resolution, which can supplement the limitations of the medium–low resolution satellite optical images.

As Arctic sea ice extent decreases dramatically (Comiso et al., 2008; Cavalieri and Parkinson, 2012), the necessity for research on the evaluation of PM SIC data around the Northern Sea Route has been emphasized to enable the discovery of more economical, faster, and safer sailing routes. Sea ice in the Chukchi Sea exhibits an earlier onset of thawing in spring and a later onset of freezing in winter, than do other regions in the Arctic Ocean (Woodgate et al., 2010). This is because the heat from the Pacific Ocean is continually transported to the Chukchi Sea through the Bering Strait. This flow moves older sea ice northwards to be replaced by newly formed ice and warms the region. Such process has intensified in recent years and has contributed to dramatic changes in the extent of sea ice and even to its thickness in the Chukchi Sea (Maslanik et al., 2007; Comiso, 2012; Stroeve et al., 2012). The heat uptake from the Pacific Ocean and warm winds from the south tend to transport water vapor into the Chukchi Sea (Serreze et al., 2016). This impacts brightness temperature of open water measured by the PM sensors and causes retrieval of erroneous SIC values (Gloersen and Cavalieri, 1986; Andersen et al., 2006; Shin et al., 2008). Meanwhile, the warm conditions in summer in the region can promote sea ice melting, which is a major source of SIC underestimation from PM measurements (Cavalieri et al., 1990; Comiso and Kwok, 1996; Ivanova et al., 2015; Kern et al., 2016). Moreover, based on the regional characteristics of sea ice in the region, the Chukchi Sea is the terminus of the Northern Sea Route, where many vessels sail in summer by laying a route using PM SIC products retrieved from the algorithms. However, only a few studies have evaluated SIC products in this region.

The sea ice variability in the Chukchi Sea is closely linked to local climate change (Overland et al., 2011; Stroeve et al., 2014) and the PM SIC products have been used as a primary data to investigate the sea ice variability (Cavalieri et al., 2003; Comiso et al., 2008; Cavalieri and Parkinson, 2012). Therefore, it is necessary to evaluate the accuracy of the PM SIC products in the Chukchi to support climate research and to benefit shipping. Furthermore, the PM SIC values derived from the algorithms have accuracy that varies according to the ranges of the values. This is because of different sensitivities of the algorithms to atmospheric effects and to ice surface conditions by the range of SIC values (Comiso et al., 1997; Ivanova et al., 2015). The weekly ice charts provided by the Russian Arctic and Antarctic Research Institute (AARI) show that the range of SIC values in the Chukchi Sea in summer (Fig. 1a) is typically wider than in winter (Fig. 1b). Therefore, thorough verification of the accuracy of the PM SIC is required for the various ranges of SIC for the region in summer.

In this study, we evaluated SICs estimated from four sea ice algorithms implemented for PM measurements, namely NT, BT, OSISAF, and ASI, using high resolution ice/water maps with high accuracy derived from KOrean Multi-Purpose SATellite-5 (KOMPSAT-5) SAR images obtained in the Chukchi Sea of the Arctic Ocean in summer. SIC values were calculated from the KOMPSAT-5 ice/water maps, which were then compared with those from the algorithms. The differences in SICs derived from KOMPSAT-5 and the sea ice algorithms were analyzed statistically using different ranges of SIC values. The relationships between the biases from the algorithms and numerical weather prediction data were analyzed in order to investigate influences of atmospheric effects and ice surface conditions on the SIC values. Section 2 presents the data used in this research. Section 3 describes the methodology for the generation of ice/water maps from the KOMPSAT-5 SAR images and for the evaluation of the SICs estimated from the sea ice algorithms. Section 4 presents the results and discussion, and Section 5 concludes this paper.

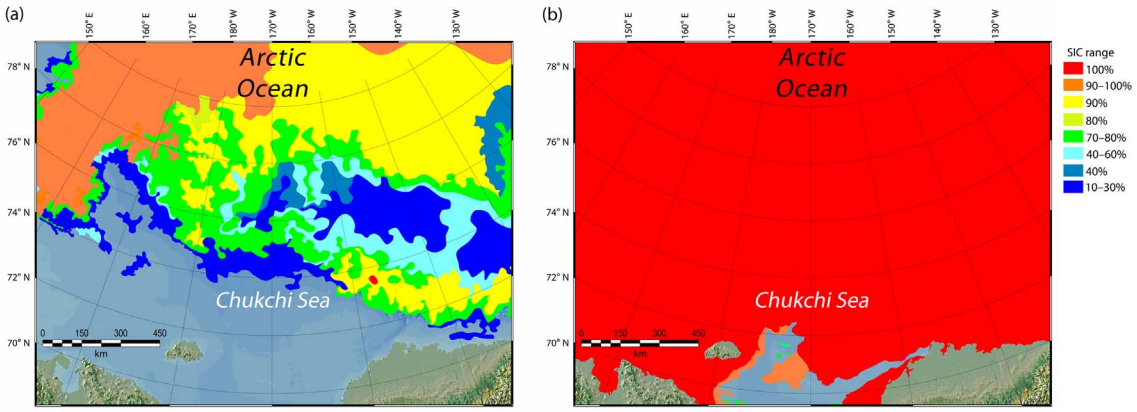

Fig. 1. Ranges of SIC values for the Chukchi Sea derived from the AARI weekly ice charts released on (a) 18 August 2015 (summer) and (b) 1 December 2015 (winter).

2. Data

2.1. KOMPSAT-5 SAR and KOMPSAT-2 MSC images

KOMPSAT-5, launched on August 22, 2013 and operated at the Korea Aerospace Research Institute (KARI) is South Korea's first satellite equipped with X-band SAR (with a center frequency of 9.66 GHz). KOMPSAT-5 acquires images in seven observation modes with different spatial resolutions: High Resolution (HR, a spatial resolution of 2.7 m at 1-look), Enhanced HR (2 m), Ultra HR (0.85 m), Standard (ST, 3 m), Enhanced ST (2.5 m), Wide Swath (WS, 20 m), and Enhanced WS (EW, 6.25 m) modes. Although the revisit period of KOMPSAT-5 is 28 days, it can observe the same area twice a day based on swath overlay. The high resolution and standard observation modes of KOMPSAT-5 cover a 5 × 5 km and 30 × 30 km area, respectively, which would not be sufficient to observe sea ice formed over a wide area. While the wide swath observation modes capture an area of 100 × 100 km, the EW observation mode provides images with a spatial resolution of 6.25 m and it is capable of mapping sea ice with high spatial resolution and high accuracy.

In this study, we used a total of 78 KOMPSAT-5 EW SAR images of the Chukchi Sea, with HH polarization, obtained from 6 August to 9 September 2015 (Fig. 2). The SAR images were acquired by tracking the location of ARAON, an ice breaking research vehicle (IBRV) operated by the Korea Polar Research Institute (KOPRI) that sailed in the Chukchi Sea from 1 to 22 August 2015. To provide sea ice images around the sailing route to ARAON rapidly, SAR images were acquired for both ascending and descending orbits at various radar incidence angles (29° to 55°). All the SAR images were delivered as ellipsoidal geocoded product with a pixel spacing of 6.25 m.

To investigate the ice surface conditions, we obtained three high-resolution optical images at the regions of different SIC in the Chukchi Sea by KOMPSAT-2 Multi Spectral Camera (MSC) on 13, 15, and 19 August 2015. KOMPSAT-2 MSC provides visible images (in red, green and blue bands) and a near-infrared image with a spatial resolution of 4 m and a panchromatic image with 1 m resolution. The imaging areas of KOMPSAT-2 MSC are indicated by white, yellow, and green boxes in Fig. 2. We generated pan-sharpened images with a spatial resolution of 1 m by combining the high-resolution detail from the panchromatic band with the lower resolution color information from the visible bands, and then investigated the ice surface conditions. The KOMPSAT-2 MSC images were not obtained simultaneously with KOMPSAT-5 SAR images. We could not obtain high-resolution satellite optical images at the same time as the KOMPSAT-5 SAR images due to heavy cloud cover over the study area during SAR image acquisition. The KOMPSAT-2 MSC images for the white and yellow boxes in Fig. 2 were obtained one day before the KOMPSAT-5 SAR images were acquired for the corresponding regions. The MSC image for the green box was obtained three days after the SAR image acquisition. Nevertheless, the KOMPSAT-2 MSC images were adequate to investigate the surface conditions of sea ice in the study area based on high-spatial resolution.

2.2. Passive microwave sea ice concentrations

The NT (Cavalieri et al., 1984), OSISAF (Breivik et al., 2001; Tonboe et al., 2016), BT (Comiso, 1986), and ASI (Spreen et al., 2008) algorithms (Table 1) have been widely used for the retrieval of SIC using SSMIS and AMSR2 measurements, of which SIC values were evaluated in this research. The SSMIS is composed of 24 channels with frequencies ranging from 19 to 183 GHz (Kunkee et al., 2008), while the AMSR2 has seven dually polarized frequencies ranging from 6.9 to 89 GHz (Okuyama and Imaoka, 2015) (Table 2). The SSMIS and AMSR2 channels have different footprint size with various frequencies.

The NT algorithm uses the tie points of first-year ice, multi-year ice, and open water to estimate SICs for the polarization ratio (PR) at the 19 GHz (19.0 GHz of SSMIS and 18.7 GHz of AMSR2, respectively) horizontally (H) and vertically (V) polarized channels, and the spectral gradient ratio (GR) of the vertically polarized channels at 19 GHz and 37 GHz (37.0 GHz of SSMIS and 36.5 GHz of AMSR2, respectively) (Tables 1 and 2) as normalized differences of the observed brightness temperature (T_B) (Cavalieri et al., 1984). The NSIDC provides NT SIC products with a grid spacing of 25 km based on footprint sizes of the SSMIS channels.

The BT algorithm estimates total ice concentration using the T_B measured at the 37 H and 37 V (polarization mode) or 19 V and 37 V (frequency mode) channels (Table 1) (Comiso, 1986). SIC values of the consolidated pack ice regions (i.e., high Arctic area) are typically determined from T_B values at the 37 H and 37 V channels. Meanwhile, the gradient difference between 19 V and 37 V channels is used for the seasonal ice area near the ice edge and open water. The BT algorithm assumes only two surface types: sea ice and open water. We used the BT SIC products with a grid spacing of 12.5 km based on AMSR2 measurements, provided by the IUP at the University of Bremen.

The OSISAF algorithm retrieves SIC by a combination of algorithms based on the BT frequency mode and Bristol algorithm, in which T_B values measured at the vertically polarized channels at 19 GHz and the dually polarized channels at 37 GHz are used (Table 1) (Breivik et al., 2001; Tonboe et al., 2016). In the OSISAF algorithm, the BT frequency mode is used over open water, while the Bristol algorithm is used over sea ice. The SIC values are estimated by an average, weighted linearly between the two algorithms at intermediate concentrations up to 40% measured from the BT frequency mode (Tonboe et al., 2016). For the estimation of higher SICs, only the Bristol algorithm is used in the OSISAF algorithm. The EUMESAT provides SIC products with a grid spacing of 10 km using the OSISAF algorithm based on the SSMIS measurements, which are used in this study.

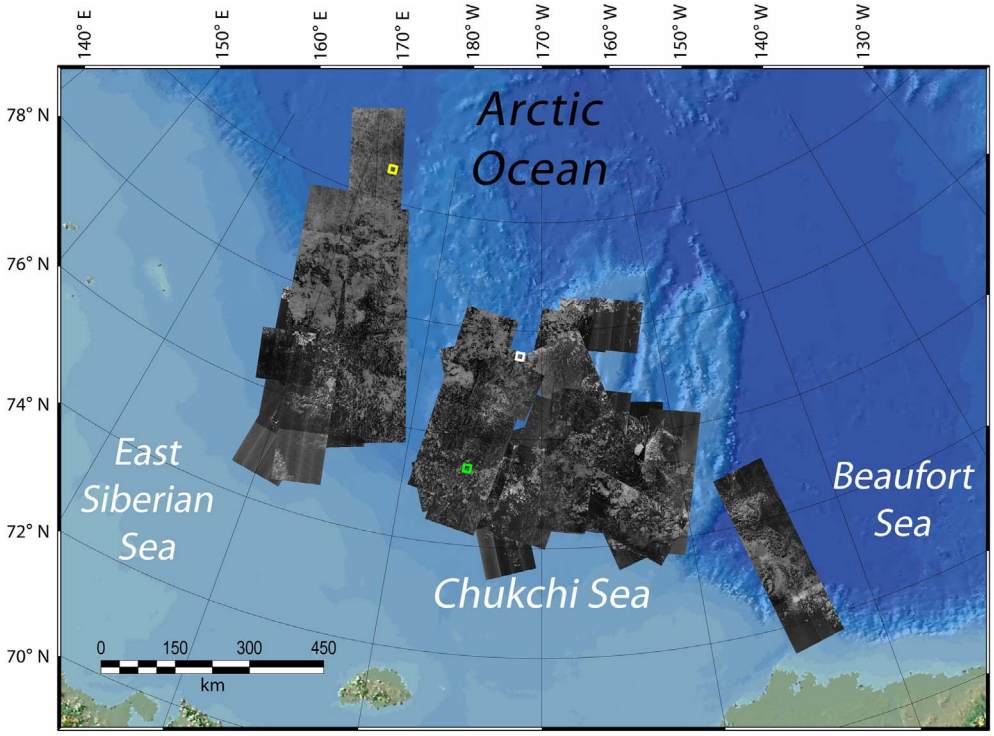

Fig. 2. A mosaic of the KOMPSAT-5 EW SAR images used in this study. The yellow, white, and green boxes represent imaging areas of KOMPSAT-2 MSC on 13, 15, and 19 August 2015. (For interpretation of the references to color in this figure legend, the reader is referred to the web version of this article.)

Table 1
Sea ice algorithms for the sea ice concentration estimates evaluated in this study.

Name	Acronym	Channels used	Grid size of SIC products (km)
NASA Team	NT	19 H, 19 V, 37 V	25
Bootstrap	BT	19 V, 37 H, 37 V	12.5
OSISAF	OSISAF	19 V, 37 H, 37 V	10
ARTIST Sea Ice	ASI	89 H, 89 V	3.125

Table 2
Frequencies and footprints of the SSMIS and AMSR2 channels used for sea ice algorithms listed in Table 1.

Frequency (GHz)	Footprint (km × km)
SSMIS	
19.3	45 × 70
22.2	40 × 60
37.0	30 × 38
85.5	14 × 16
91.7	13 × 16
AMSR2	
18.7	14 × 12
23.8	15 × 26
36.5	7 × 12
89.0	3 × 5

The ASI algorithm uses the difference of dually polarized T_B values measured at high frequency channels (89 GHz of AMSR2) to retrieve SIC values (Table 1) (Spreen et al., 2008). Sea ice shows small differences between the T_B measured at 89 V and 89 H, while open water shows large differences. Because high frequency channels are used, the ASI algorithm is sensitive to weather conditions. It also offers SIC products with finer spatial resolution than other algorithms employing lower frequency channels (Table 1). Moreover, the T_B values measured at high frequency channels are potentially less influenced by the snow layer on the ice surface than those at lower frequencies. The IUP provides ASI SIC products with grid sizes of both 6.25 km and 3.125 km. In this study, we used ASI SIC products with a grid size of 3.125 km produced by the IUP.

In most sea ice algorithms, the presence of atmospheric water content, cloud liquid water, and wind-roughened water surface are major sources of false indications of sea ice. To remove the misidentification of sea ice due to atmospheric effects, the algorithms, except for the OSISAF algorithm, use the same weather filters based on T_B values measured at the 19 V, 22 V, and 37 V channels (Gloersen and Cavalieri, 1986; Cavalieri et al., 1995; Spreen et al., 2008). The weather filters can reduce atmospheric effects during the retrieval of the SICs. However, they can overestimate SIC values for regions with low SICs or new ice, especially at the ice edge (Andersen et al., 2006). The spatial resolutions of the 19 V, 22 V, and 37 V channels used in the weather filters are lower than the grid size of ASI SIC product (3.125 km), which can lead to overestimation of SIC near ice edges owing to lack of coverage by weather filters (Spreen et al., 2008). The OSISAF uses information about atmospheric conditions such as atmospheric water vapor content, cloud liquid water and air temperature derived from a radiative transfer model to reduce weather impacts on the measured T_B values (Tonboe et al., 2016).

2.3. ERA-Interim reanalysis data

Atmospheric water vapor, cloud liquid water and wind-roughened open water surface can increase the T_B over open water, and are the major sources of overestimation of SIC by the sea ice algorithms, especially in regions of low SIC (Gloersen and Cavalieri, 1986; Andersen et al., 2006). Meanwhile, ice surface melting is the main cause of underestimation of SIC by the algorithms because it decreases T_B over sea ice (Ivanova et al., 2015). To analyze the influences of atmospheric effects and ice surface melting on the SIC values from the algorithms, the total columnar water vapor (TCWV), total cloud liquid water (TCLW), 10 m wind speed, and air temperature at the 925 hPa pressure level were used. These were part of the numerical weather prediction (NWP) data in the European Reanalysis Agency (ERA)

Interim reanalysis products (Dee et al., 2011). The ERA Interim provides multi-decadal (from 1979 to present) reanalysis fields of global integrated and coherent climate observation by using a data assimilation system, and it has been widely used to investigate the influences of atmospheric conditions on sea ice variability (Screen and Simmonds, 2010; Cuzzone and Vavrus, 2011; Serreze et al., 2016). The grid resolution of the ERA Interim reanalysis data is 0.75° in latitude × 0.75° in longitude with 60 vertical pressure levels from ground to 0.1 hPa.

The TCWV and 10 m wind speed was provided as 3-hourly fields from the ERA Interim reanalysis, while the TCLW was provided as 6-hourly fields. As daily SIC products from the sea ice algorithms were used, the reanalysis fields were averaged daily. In summer, the use of air temperature at 925 hPa is preferred over the surface air temperature (i.e., 2 m air temperature provided by the ERA Interim) to investigate ice surface conditions. This is because the surface air temperature in summer is constant regardless of thermal energy input, while the air temperature at 925 hPa indicates the thermal state of the lower troposphere and thus is appropriate to help assess ice surface melting (Serreze et al., 2016). High air temperature at 925 hPa in summer (June–August) can promote sea ice melting (Serreze et al., 2003). In this research, the values of the air temperature at 925 hPa were averaged from June to July 2015 because the KOMPSAT-5 SAR images were obtained from August–September 2015. These were used to investigate the influence of ice surface melting on the SIC values provided by the algorithms. Fig. 3a and b shows the Arctic June–July mean air temperature at 925 hPa from 1979 to 2014 and the June–July mean air temperature anomalies in 2015. The anomalies were calculated with respect to the period June–July of 1979–2014. The black dotted box in Fig. 3 corresponds to the KOMPSAT-5 SAR imaging coverage shown in Fig. 2. In 2015, the mean June–July air temperature over the Chukchi Sea was 1–4 °C higher than during 1979–2014. Such positive anomalies were potentially caused by the increasing uptake of ocean heat flux from the Pacific Ocean by the Bering Strait and the seasonal ice/ocean albedo feedback in spring (Woodgate et al., 2010; Serreze et al., 2016), which could promote ice surface melting later (i.e., August and September).

The wind speed and air temperature measured by the meteorological sensor mounted on the IBRV ARAON could not be used because the distance between the KOMPSAT-5 SAR imaging area and the IBRV was > 100 km, except for a few SAR images. Moreover, the KOMPSAT-5 SAR images were acquired from 6 August to 9 September 2015 but the voyage of the IBRV ARAON ended on 22 August 2015.

3. Methodology

This section describes the methods for generating ice/water maps from KOMPSAT-5 EW SAR images using a machine learning-based binary classification. The methods for statistical evaluation of SIC values estimated from the algorithms using the KOMPSAT-5 ice/water maps are also presented. Fig. 4 shows the data processing flows for this study.

3.1. Generation of KOMPSAT-5 ice/water maps

To retrieve SIC values from the KOMPSAT-5 EW SAR images, we generated ice/water maps using a sea ice mapping model developed by Han et al. (2017). The sea ice mapping model classifies a KOMPSAT-5 EW SAR image into sea ice and open water based on a binary classification of various SAR texture features by Random Forest (RF). RF is a rule-based machine learning approach (Breiman, 2001) that has been widely used for various remote sensing applications including land cover/land use classification (Hayes et al., 2014; Rhee et al., 2014; Torbick and Corbiere, 2015), vegetation mapping (Li et al., 2013; Long et al., 2013; Kumar and Sinha, 2014; Immitzer et al., 2016), oceanographic and hydrologic studies (Y.H. Kim et al., 2014; Liu et al., 2015; Song et al., 2015), atmospheric research (Han et al., 2015; Lee et al., 2017), and sea ice mapping (Kim et al., 2015; Han et al., 2016; Han et al., 2017). RF makes rule-based classification trees by generating multiple bootstrapped samples of the original training data and creating a series of no-pruning classification and regression trees (CART) that are non-parametric decision trees (Breiman, 2001). Independent trees are grown by a randomly selected subset of the training samples for each tree and a randomly selected subset of splitting variables at each node of the tree. These processes overcome a key limitation of CART, which is that classification results are greatly influenced by the configuration and quality of training samples. RF produces the relative importance of input variables by the mean decrease accuracy (MDA), which is the average increase in the misclassification rate as a

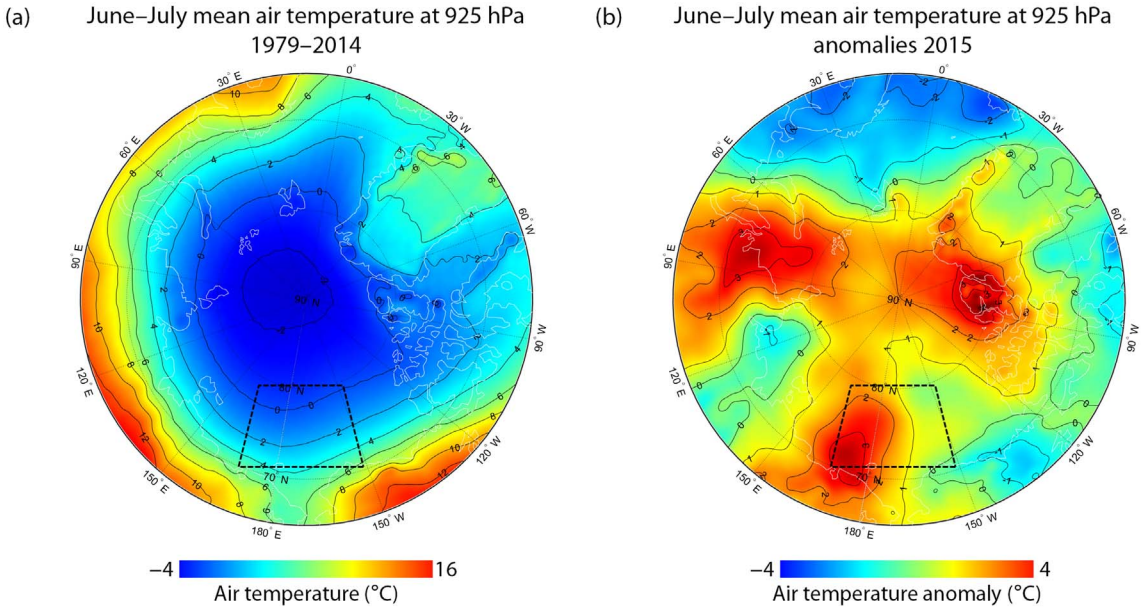

Fig. 3. (a) Arctic June–July mean air temperature at 925 hPa during 1979–2014. (b) June–July mean air temperature anomalies in 2015, which were calculated with respect to 1979–2014. The white lines represent coastline and the black lines indicate the contours of values. The black dotted box corresponds to the coverage by KOMPSAT-5 SAR images of the Chukchi Sea.

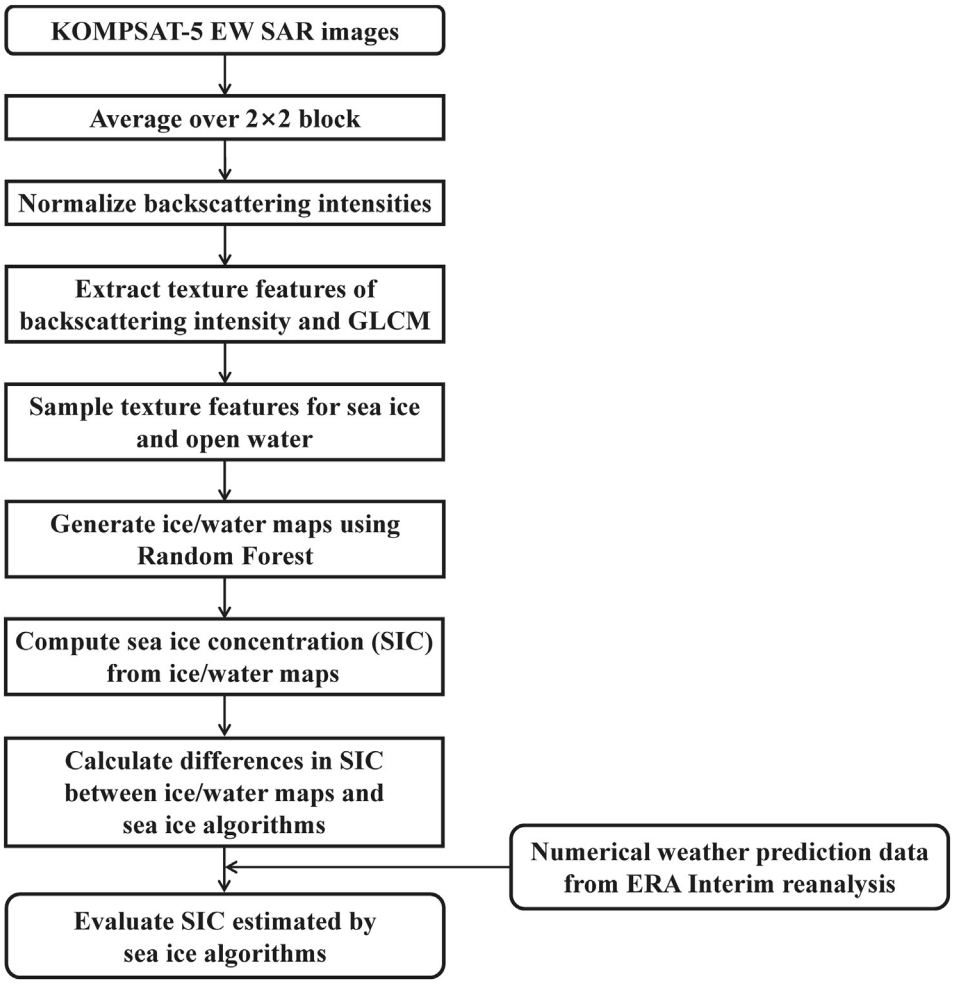

Fig. 4. Processing flow of the evaluation of SIC estimated by sea ice algorithms based on the KOMPSAT-5 ice/water maps.

percentage. RF trains quickly and outperforms artificial neural networks when faced with a limited number of training samples and a large number of input variables (Cracknell and Reading, 2014).

In the sea ice mapping model, a total of 12 texture features computed from the KOMPSAT-5 EW SAR images—average, standard deviation, minimum, and maximum values of the backscattering intensity, and energy, entropy, correlation, contrast, homogeneity, autocorrelation, dissimilarity, and maximum probability of the gray-level co-occurrence matrix (GLCM) were used as input variables (Han et al., 2017). The GLCM is described by

$$S_{d,\alpha}(i,j) = P_{d,\alpha}(i,j) / \sum_{i=0}^{k-1}\sum_{j=0}^{k-1} P_{d,\alpha}(i,j) \quad (1)$$

where $S_{d,\alpha}$ is an element of GLCM, $P_{d,\alpha}$ is the number of neighbor pixel pairs separated by a pixel distance d (called the interpixel distance), k is the number of quantized gray-levels in the image, and α is the orientation of the pixel pairs (Haralick et al., 1973; Soh and Tsatsoulis, 1999; Zakhvatkina et al., 2013). Each element (i,j) of the GLCM represents the probability that two pixels, separated by an interpixel distance, have gray levels i and j. The number of rows and columns of the GLCM is equal to the number of gray-levels. The optimal number of gray-levels typically used is 16, which is efficient for the calculation time of texture features and sufficient to represent textures for classification (Soh and Tsatsoulis, 1999; Zakhvatkina et al., 2013). Averaging the GLCM for four directions (α of 0°, 45°, 90°, and 135°) is preferred for recognizing the position and possible rotation of the sea ice (Clausi, 2002). Table 3 shows the formulas of the GLCM texture features (Soh and Tsatsoulis, 1999) used in this study.

Table 3
Formulas of the GLCM texture features (Soh and Tsatsoulis, 1999).

Texture feature	Formula
Energy	$\sum_{i=0}^{k-1}\sum_{j=0}^{k-1} S(i,j)^2$
Entropy	$-\sum_{i=0}^{k-1}\sum_{j=0}^{k-1} \ln(S(i,j))S(i,j)$
Correlation	$\sum_{i=0}^{k-1}\sum_{j=0}^{k-1} \frac{(ij)S(i,j)-\mu_x\mu_y}{\sigma_x\sigma_y}$ where μ_x, μ_y, σ_x, and σ_y denote the mean and standard deviations of the row and column sums of the GLCM, respectively.
Contrast	$\sum_{n=0}^{k-1} n^2 \left\{ \sum_{i=1}^{k}\sum_{j=1}^{k} S(i,j) \,\middle|\, \lvert i-j\rvert = n \right\}$
Homogeneity	$\sum_{i=0}^{k-1}\sum_{j=0}^{k-1} \frac{S(i,j)}{1+(i-j)^2}$
Autocorrelation	$\sum_{i=0}^{k-1}\sum_{j=0}^{k-1} (ij)S(i,j)$
Dissimilarity	$\sum_{i=0}^{k-1}\sum_{j=0}^{k-1} \lvert i-j\rvert\, S(i,j)$
Maximum probability	$\max_{i,j} S(i,j)$

The texture features derived from SAR intensity and the GLCM have been widely used for sea ice detection from SAR images because they

contain information on the spatial distribution of backscattering, which differs substantially between sea ice and open water (Soh and Tsatsoulis, 1999; Clausi, 2001; Zakhvatkina et al., 2013; Leigh et al., 2014; Ressel et al., 2015; Han et al., 2016; Han et al., 2017). KOMPSAT-5 EW SAR images were acquired at various incidence angles, so that the values of texture features over sea ice and open water computed from the backscattering intensity itself could vary as a function of the incidence angle (Mäkynen and Hallikainen, 2004; Ressel et al., 2015; Pogson et al., 2017). In particular, open water can show similar or higher backscattering than sea ice under strong wind conditions, which is noticeable at low incidence angle (Ressel et al., 2015; Pogson et al., 2017). In C-band HH-polarized SAR image, open water can show higher backscattering than sea ice at incidence angle below 35° under strong wind condition (Pogson et al., 2017). The KOMPSAT-5 SAR is in X-band, which has shorter wavelength than the C-band, and the observed backscattering is more sensitive to the surface roughness. However, the wind conditions have little effects on the backscattering in X-band at high incidence angles (> 30°) (Ressel et al., 2015). As the KOMPSAT-5 SAR images were acquired at the incidence angle higher than 29°, we computed the texture features from the normalized SAR intensity values by assuming that the backscattering of sea ice is typically stronger than that of open water, regardless of the incidence angle. Prior to the computation of texture features, a 2 × 2 block averaging of the normalized SAR images was performed to reduce speckle noise.

Han et al.'s (2017) sea ice mapping model adopted texture features computed using a 10 × 10 non-overlapping pixel window and a *d* value of 1. A total of 84,000 samples (i.e., elements of a texture) were extracted by visual inspection from the SAR images (42,000 samples for sea ice and 42,000 samples for open water). Seventy percent of the total samples were randomly extracted and used as a training dataset, while the remaining samples were used as a test dataset to validate the sea ice mapping model. The non-overlapping and even-numbered (10 × 10) pixel window used by Han et al. (2017) has a disadvantage in spatial resolution of the resulting ice/water maps compared to an odd-numbered sliding pixel window. Nevertheless, it contributed to efficiency in the computational costs of texture features from the SAR images, and the accuracy of the resulting maps was very high. In this study, we generated ice/water maps using the same KOMPSAT-5 EW SAR images, data processing flow, and RF-based sea ice mapping model presented in Han et al. (2017). The KOMPSAT-5 ice/water map has a grid size of 125 m, which inherits the grid size of texture features determined by a 10 × 10 non-overlapping pixel window for the 2 × 2 block averaged SAR intensities with a grid spacing of 6.25 m. As we used the same SAR images and sea ice mapping model as Han et al. (2017), the ice/water maps have the same accuracy in sea ice mapping as reported in that study (Table 4). The ice/water maps showed very high overall accuracy and Kappa coefficient (99.24% and 98.48%, respectively). The user's and producer's accuracies for sea ice (99.64% and 98.83%, respectively) and for open water (98.84% and 99.64%, respectively) were found to be very high, as well. Such high performance in the sea ice and open water mapping is due to the superior classification strategy of RF and to the striking differences in the texture features of ice and water

Table 4
Accuracy assessment of the KOMPSAT-5 sea ice mapping model based on Random Forest (Han et al., 2017).

Classified as	Reference			
	Sea ice	Open water	Row total	User's accuracy (%)
Sea ice	12,453	44	12,497	99.64
Open water	147	12,556	12,703	98.84
Column total	12,600	12,600	25,200	
Producer's accuracy (%)	98.83	99.65		
Overall accuracy (%)	99.24			
Kappa coefficient (%)	98.48			

(Han et al., 2016; Han et al., 2017). Han et al. (2017) evaluated the performance of the sea ice and open water classification from the sea ice mapping model by comparing the SICs of the model-derived ice/water maps with those of the AARI weekly ice charts. They reported that the SICs derived from the sea ice mapping model showed a mean difference of −8.6% with a standard deviation of 11.6% (range of the difference: −35.8% to 30.1%) from SIC values in the ice charts. Such difference was mainly attributed to the uncertainty of the SICs in the ice charts, which are typically provided as a range of values that can span up to 20% and possibly occurring at times different from the KOMPSAT-5 SAR image acquisition. As the ice charts are weekly products, the maximum difference in time between the ice charts and the KOMPSAT-5 SAR image acquisitions was 3.5 days. Therefore, SIC values derived from the KOMPSAT-5 ice/water maps can be used as reliable validation data for the SICs from the sea ice algorithms implemented for PM measurements.

3.2. Statistical evaluation of PM SICs

The SIC data products from the four sea ice algorithms have different grid sizes. The BT, OSISAF, and ASI SIC data were resampled to 25 km using the nearest-neighbor scheme to match the grid size of the NT SIC product. From the KOMPSAT-5 ice/water maps, SIC was calculated in a 20 × 20 pixel window corresponding to a grid size of 25 × 25 km where the area overlapped with the PM SIC. Values of the correlation coefficient (*R*), mean bias (mean error), standard deviation of errors (SE), and root mean square error (RMSE) of SICs from the algorithms were computed by comparing with the SICs from the KOMPSAT-5 ice/water maps. Errors in the SICs from the algorithms were calculated by subtracting the corresponding values from the ice/water map. We also performed a paired sample *t*-test at the 95% confidence level to investigate whether there were statistically significant differences between the SIC values retrieved from the sea ice algorithms and from the KOMPSAT-5 ice/water maps.

The sea ice algorithms can retrieve different values from varied ranges of SIC values owing to the use of different channels and indices for SIC estimation. In this study, we defined three sea ice regions based on different SIC thresholds computed from the KOMPSAT-5 ice/water maps: an open drift ice zone (ODIZ) corresponding to KOMPSAT-5 SICs ranging from 0% to 15%, a marginal ice zone (MIZ) corresponding to KOMPSAT-5 SICs ranging from 15% to 80%, and a consolidated pack ice zone (CPIZ) corresponding to KOMPSAT-5 SICs ranging from 80% to 100% (Stroeve et al., 2016). Statistical analyses of the SIC values estimated by the algorithms were performed for four cases: one for all SIC ranges, the second for the ODIZ, the third for the MIZ, and the last for the CPIZ. We also compared the SICs estimated from the algorithms for all SIC ranges, the ODIZ, the MIZ, and the CPIZ.

A positive bias of SIC from the algorithms means that the open water concentration (OWC) was underestimated compared to that derived from the KOMPSAT-5 SAR. Meanwhile, a negative bias from the algorithms suggests that SIC was underestimated. In this research, the false negative ratio of open water (FNR_{OW}) and sea ice (FNR_{SI}) was considered for investigating the influences of atmospheric effects and ice surface conditions on the biases of PM SICs. The FNR_{OW} is the ratio of underestimated PM OWC to KOMPSAT-5 OWC, while FNR_{SI} is the ratio of underestimated PM SIC to KOMPSAT-5 SIC. The terms FNR_{OW} and FNR_{SI} are computed as

$$FNR_{OW} = (\mathrm{PM\,SIC} - \mathrm{K5\,SIC})/\mathrm{K5\,OWC} \quad \text{for}\ \mathrm{K5\,SIC} < \mathrm{PM\,SIC} \tag{2}$$

$$FNR_{SI} = (\mathrm{K5\,SIC} - \mathrm{PM\,SIC})/\mathrm{K5\,SIC} \quad \text{for}\ \mathrm{K5\,SIC} > \mathrm{PM\,SIC} \tag{3}$$

where K5 SIC and K5 OWC are the SIC and OWC computed from the KOMPSAT-5 ice/water maps, respectively. The FNR_{OW} and FNR_{SI} have values ranging from 0 to 1. The calculated value of FNR_{OW} (or FNR_{SI}) is 1 when the algorithm detects open water (or sea ice) correctly, and the calculated value is 0 if open water (or sea ice) is completely

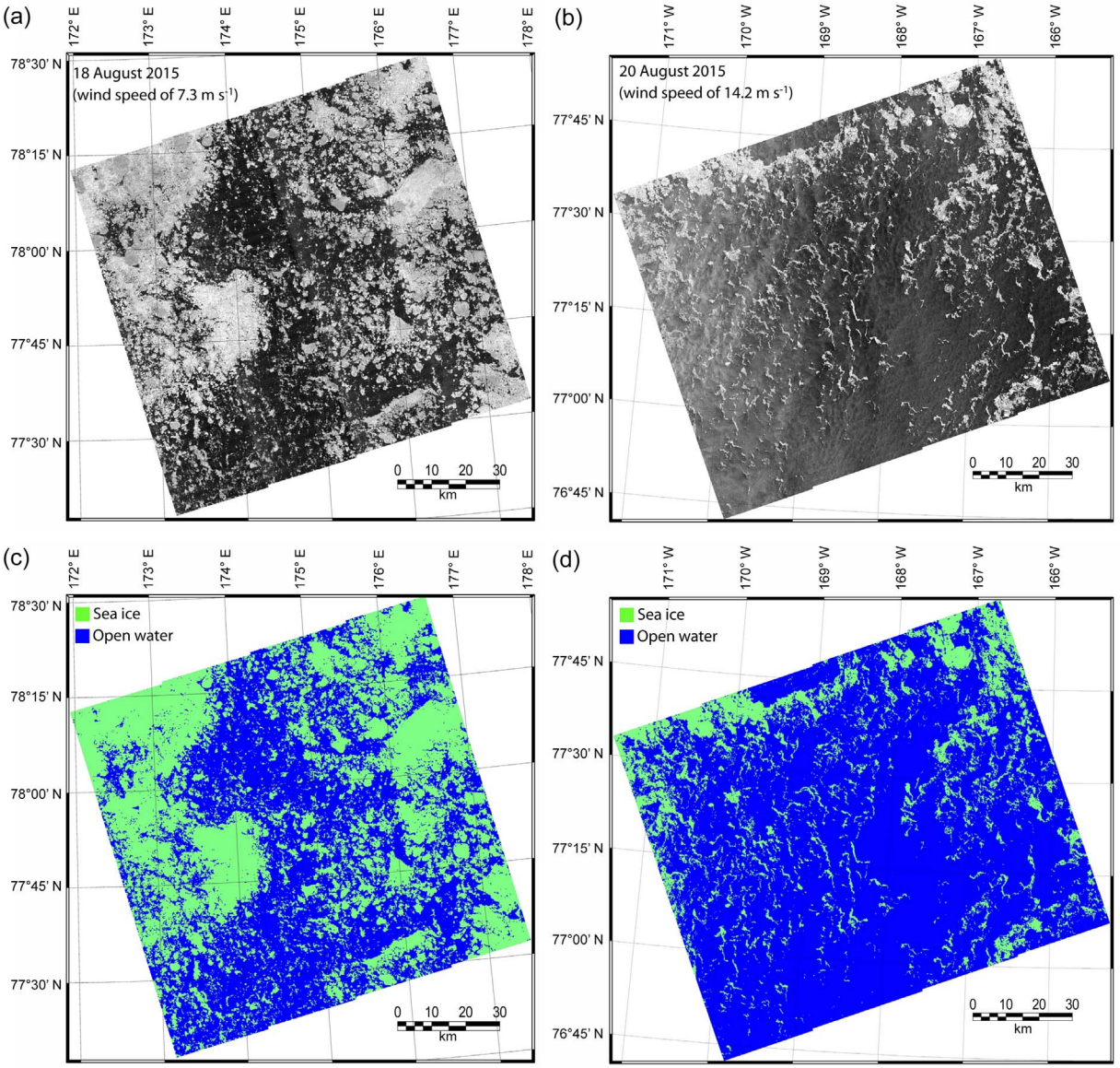

Fig. 5. Examples of (a and b) KOMPSAT-5 EW SAR images and (c and d) corresponding ice/water maps under different wind conditions. The wind speed was measured by a meteorological sensor mounted on IBRV ARAON, which sailed near the SAR imaging area (but was not captured in the images) at the image acquisition time.

misinterpreted (as its opposite) in the algorithm. The values of FNR_{OW} and FNR_{SI} from the algorithms were compared with the daily averaged TCWV, TCLW and 10 m wind speed on the same day and location as the PM SICs, and with the June–July 2015 mean air temperature at 925 hPa at the same location as the grids of the PM SICs.

4. Results and discussion

Ice/water maps were generated from the KOMPSAT-5 EW SAR images using the RF-based sea ice mapping model. Examples of the ice/water maps are shown in Fig. 5. The wind speeds presented in Fig. 5 were measured by a meteorological sensor mounted on the IBRV ARAON. The IBRV ARAON was not captured in the SAR images and was located about 50 km away from the imaging regions. The location of IBRV ARAON was 77° 0′ 46″ N, 179° 58′ 53″ W and 75° 54′ 29″ N, 168° 55′ 33″ W at the acquisition time of Fig. 5a and b, respectively. Nevertheless, the wind speed measured at the IBRV ARAON could be used to account for ocean surface conditions in the SAR images because the spatial variation of wind speed would be insignificant. The 10 m wind speed predicted by the ERA Interim data was 4.8 m s^{-1} and 5.2 m s^{-1} for the center location at the closest time of the SAR image acquisitions, which is a large deviating from the wind speed measured at the IBRV ARAON. The SAR image acquisition time for Fig. 5a and b was 17:29 UTC and 15:46 UTC, respectively, on the same day. As the 10 m wind speed from the ERA Interim is provided in 3-hourly fields, there was a time difference longer than 30 min between the SAR image acquisitions and the wind speed predictions. The temporal variation of wind speed is expected to be larger than its spatial variation. Therefore, the wind speed measured at the IBRV ARAON would be more suitable for explaining the ocean surface conditions in the target areas. The ice/water maps could discriminate between the sea ice and open water, even for the SAR image including wind-induced rough water in regions with low SICs (Fig. 5c and d). This is because of the distinct texture features of sea ice and open water, and the excellent classification performance by RF (Han et al., 2017). Sea ice areas below 125 × 125 m were misclassified as open water in the ice/water maps because the ice floes were not large enough to compute texture features indicating sea ice. Therefore, SIC values derived from the KOMPSAT-5 ice/water maps were slightly underestimated compared to visual observations of the SAR images, especially for the ODIZ, where very small ice fragments are

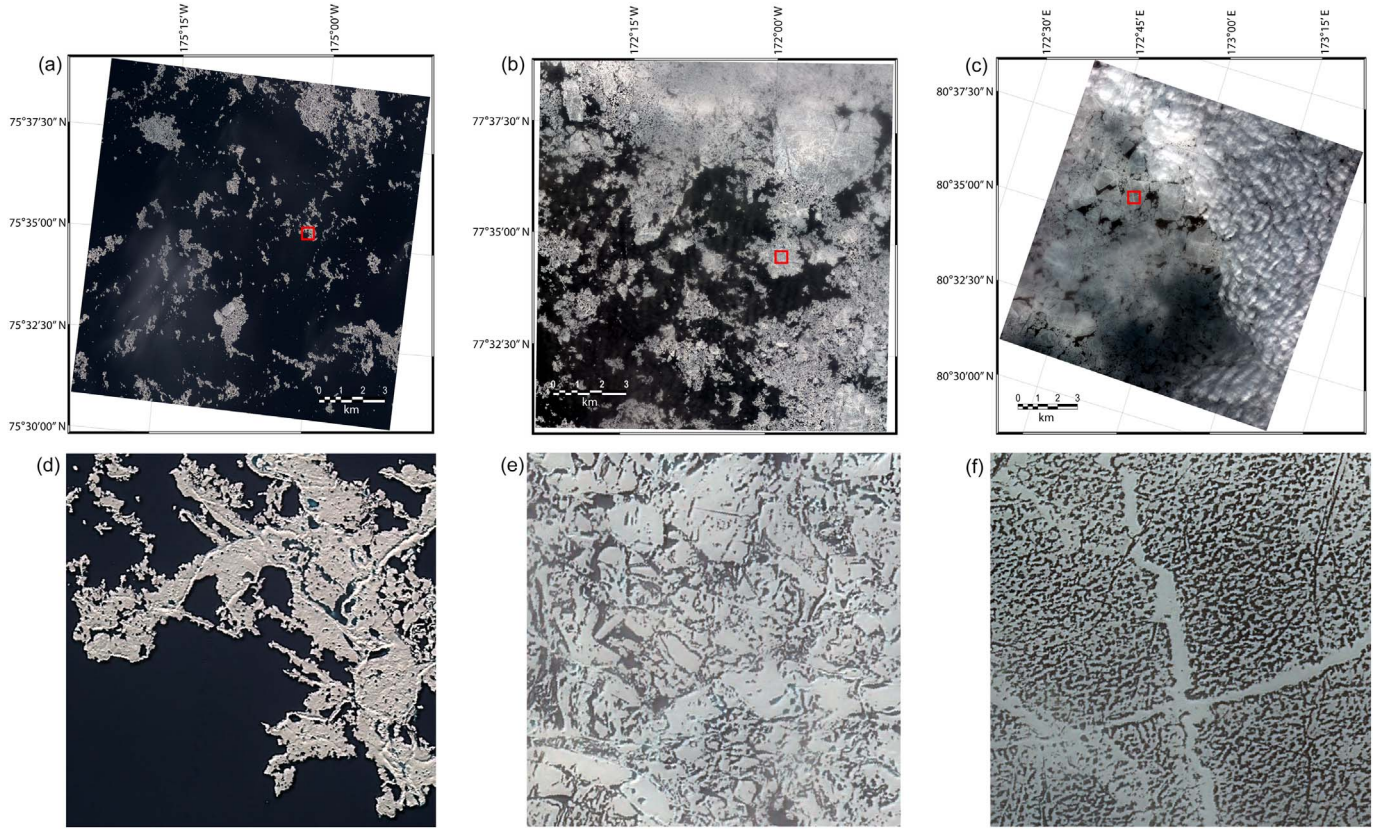

Fig. 6. KOMPSAT-2 MSC images obtained for (a) the ODIZ on 19 August 2015, for (b) the MIZ on 15 August 2015, and for (c) the CPIZ on 13 August 2015. (d, e and f) Enlarged images corresponding to the red box in (a), (b) and (c), respectively. (For interpretation of the references to color in this figure legend, the reader is referred to the web version of this article.)

common. The KOMPSAT-2 MSC image, with a spatial resolution of 1 m, obtained for the ODIZ on 19 August 2015 (Fig. 6a and d) shows that the area of sea ice in this region was very small.

A total of 631 SIC values were derived from the KOMPSAT-5 ice/water maps. Fig. 7 shows the distribution of the values computed from the ice/water maps, for which the ODIZ, MIZ, and CPIZ are represented in blue, green, and red colors, respectively. Approximately 90% of the KOMPSAT-5 SIC values were extracted for the ODIZ (310 values) and MIZ (262 values). The number of SIC values for the CPIZ was 59, far less than that for the ODIZ and MIZ. The required number of SIC values for both parametric and nonparametric tests for comparing two paired samples was determined to be > 35 by power analysis conducted in G*Power (Faul et al., 2007) using an effect size of 0.5, an alpha of 0.05 and a power of 0.8. Therefore, the number of SIC values for the CPIZ was sufficient to statistically evaluate the values retrieved from the sea ice algorithms for the Chukchi Sea in summer.

4.1. Summary statistics of the PM SIC evaluation

Prior to statistical evaluation of the SIC values from the sea ice algorithms, we investigated the normality of SIC values from the algorithms and KOMPSAT-5 ice/water maps for the cases in all the SIC

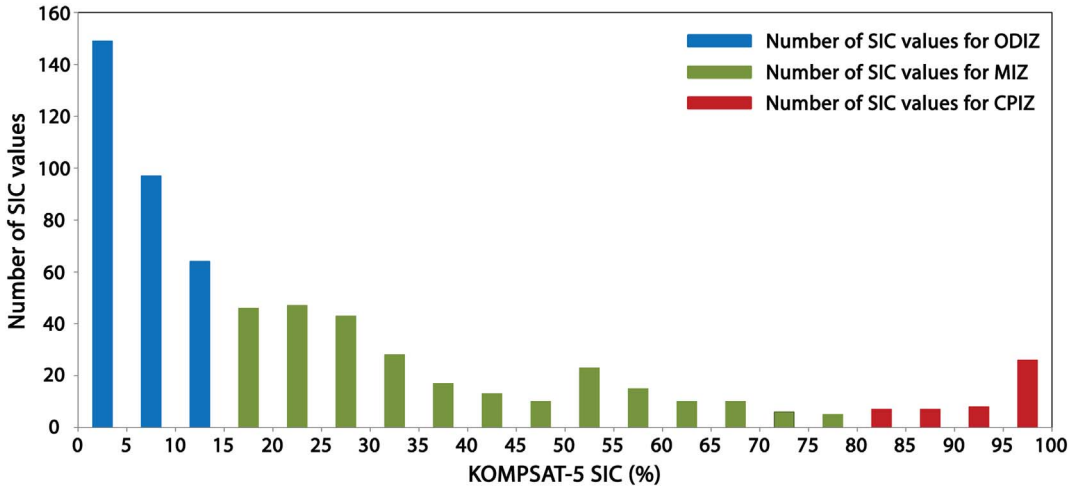

Fig. 7. Distributions of KOMPSAT-5 SIC values. Those corresponding to the OPIZ, MIZ, and CPIZ are shown in blue, green, and red, respectively. (For interpretation of the references to color in this figure legend, the reader is referred to the web version of this article.)

Table 5
Descriptive statistics of SIC values from KOMPSAT-5 and sea ice algorithms for all SIC ranges, as well as for the ODIZ, MIZ, and CPIZ.

SIC data		Mean (%)	Median (%)	CV	Min. (%)	Max. (%)	Skewness	Kurtosis	K–S
All SIC ranges	KOMPSAT-5	25.63	15.81	1.04	1.02	99.97	1.37	0.95	ns
	NT	23.58	19.2	0.81	0.00	86.25	1.07	0.78	ns
	BT	38.23	37.47	0.76	0.00	100.00	0.53	−0.54	ns
	OSISAF	27.45	20.66	0.89	0.00	100.00	1.48	1.59	ns
	ASI	32.16	25.13	0.87	0.00	98.40	0.57	−0.91	ns
ODIZ	KOMPSAT-5	6.18	5.20	0.65	1.02	14.92	0.52	−0.95	ns
	NT	10.77	11.00	0.77	0.00	42.00	0.37	−0.85	ns
	BT	16.31	13.00	0.88	0.00	56.14	0.55	−0.80	ns
	OSISAF	11.60	10.83	0.67	0.00	53.32	0.89	1.95	ns
	ASI	10.54	6.43	1.17	0.00	69.97	1.78	3.51	ns
MIZ	KOMPSAT-5	35.81	30.12	0.47	15.21	79.54	0.76	−0.53	ns
	NT	30.31	28.80	0.42	0.00	68.00	0.38	0.07	ns
	BT	53.25	50.17	0.36	0.00	100.00	0.34	0.68	ns
	OSISAF	35.18	31.17	0.53	1.53	97.81	1.29	1.90	ns
	ASI	47.44	48.09	0.41	2.87	87.44	−0.03	−1.01	ns
CPIZ	KOMPSAT-5	93.44	95.93	0.06	81.13	99.97	−0.78	−0.74	ns
	NT	67.78	70.80	0.15	41.20	82.40	−1.15	0.60	ns
	BT	94.96	98.18	0.08	77.10	100.00	−1.52	0.79	ns
	OSISAF	85.85	87.31	0.17	46.89	100.00	−1.01	0.25	ns
	ASI	84.91	84.64	0.09	68.88	98.40	0.01	−0.63	*

CV: coefficient of variation; K–S: Kolmogorov–Smirnov test ($p = 0.05$), where (*) indicates that the dataset fits a normal distribution while (^{ns}) indicates that the dataset significantly deviates from a normal distribution.

regions, ODIZ, MIZ, and CPIZ based on the Kolmogorov–Smirnov (K–S) test (Lilliefors, 1967) at a probability level of 95%. SIC values from all algorithms and KOMPSAT-5 for all cases, except SIC values for the CPIZ estimated from the ASI algorithm, showed *p*-values lower than 0.05 and did not follow a normal distribution (Table 5). This means that the SIC values should be evaluated by non-parametric statistical analyses. Therefore, we computed the Spearman correlation coefficient (Pirie, 2006) and performed a Wilcoxon signed rank test (a nonparametric statistical hypothesis test used when comparing two paired samples) (Wilcoxon, 1945). The SIC values retrieved from the sea ice algorithms and KOMPSAT-5 showed vastly different descriptive statistics such as mean, median, maximum value, standard deviation, skewness, and kurtosis (Table 5).

Comparisons of SIC values estimated from the algorithms and KOMPSAT-5 for all SIC ranges are shown in Fig. 8. The vertical lines in each scatter plot correspond to KOMPSAT-5 SIC values of 15% and 80%, respectively, which were the thresholds used for separating ice regions into the ODIZ, MIZ, and CPIZ. The *Z*-statistic and *p*-value, which determine whether there is a statistically significant difference between the given two datasets in each scatter plot, were derived from the Wilcoxon signed rank test at a confidence level of 95%. The critical values of the *Z*-statistic to determine the difference between two datasets varies depending on the number of samples. Meanwhile, *p*-values below 0.05 mean that there is a statistically significant difference between the two datasets at a confidence level of 95%. All algorithms estimated a strong correlation between SIC values and KOMPSAT-5 SIC values (*R* values higher than 0.8). However, the results of the Wilcoxon signed rank test indicated statistically significant differences between the SIC values retrieved from the algorithms and those from KOMPSAT-5. The values of SE and RMSE were higher than 10% for all algorithm-retrieved SIC values, which were positively biased compared to the SIC values from KOMPSAT-5 (i.e., overestimation of SIC), except for the NT SIC values, which were slightly negatively biased (Fig. 8a).

SIC values retrieved from the BT algorithm and KOMPSAT-5 showed the highest correlation coefficient (0.91), while BT SIC values had the largest positive bias (12.64%) and showed the largest RMSE (17.93%) (Fig. 8b). Meanwhile, the comparison between the OSISAF and KOMPSAT-5 SIC values showed the lowest RMSE and bias (11.22% and 1.82%, respectively) (Fig. 8c). SIC values retrieved from the ASI algorithm showed the second highest *R* value (0.90%) (Fig. 8d). However, they showed the second largest RMSE (15.17%) and the largest SE (13.70%), which was due to the large deviation in SIC values from KOMPSAT-5 within an SIC range from 10% to 60%.

The scatter plots of Fig. 8 and the descriptive statistics of Table 5 intuitively show that SIC values retrieved from the sea ice algorithms have different biases and errors according to the range of SIC values. This is mainly attributed to different channels and principles for identifying sea ice and open water in the algorithms and to the different surface emissivity for different SIC ranges. Moreover, the algorithms can show different performance of SIC retrieval due to the presence of melt ponds, leads, thin ice, and surface effects on ice and water. In the following section, we present and discuss the different performance of the algorithms for different ranges of SIC.

4.2. Evaluation of PM SICs according to KOMPSAT-5 SIC range

In this section, we report the results of statistical comparisons of SIC values from the KOMPSAT-5 ice/water maps with those from the sea ice algorithms for the ODIZ, MIZ and CPIZ, respectively. The biases of the algorithms were investigated. The contributions of atmospheric conditions expected to affect the biases and differences in the PM SICs are discussed in Section 4.3.

4.2.1. Open drift ice zone

The SIC values retrieved from all sea ice algorithms in the ODIZ were positively biased and significantly different from the KOMPSAT-5 SIC values (Table 6). The values of BT SIC showed the greatest bias (10.14%) and the largest value of RMSE (15.64%) compared to the KOMPSAT-5 SIC values. The second largest value of RMSE was computed between the ASI and KOMPSAT-5 SIC values (11.03%). The NT and OSISAF algorithms-derived SIC values showed similar RMSE values (8.44% and 8.29%, respectively).

The major source of the positive biases from the algorithms can be attributed to atmospheric effects such as atmospheric water vapor, cloud liquid water, and the wind-induced rough surface of open water (Gloersen and Cavalieri, 1986; Andersen et al., 2006; Shin et al., 2008). The weather in the ODIZ is prone to short-term changes (Cavalieri et al., 1995), especially in the Arctic summer. Atmospheric effects over open water increase T_B (Andersen et al., 2006), which is a reason for the overestimation of SIC by the algorithms. The positive biases from all algorithms were predominantly observed in the regions with KOMPSAT-5 SIC lower than 40% (Fig. 8), which could be mainly

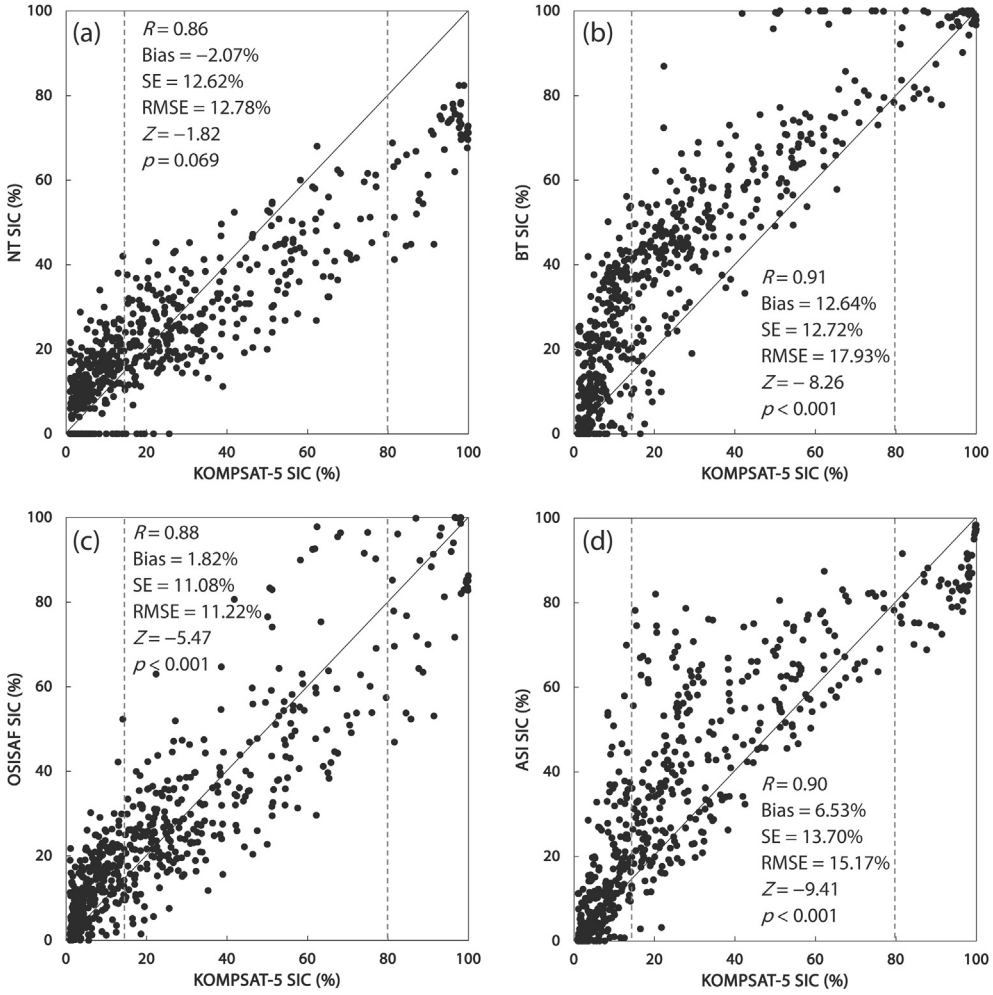

Fig. 8. Comparisons of SIC values estimated from KOMPSAT-5 with those from the algorithms (a) NT, (b) BT, (c) OSISAF, and (d) ASI. The vertical dotted lines in each scatter plot correspond to KOMPSAT-5 SIC values of 15% and 80%, respectively.

Table 6
Comparison of SIC values estimated from KOMPSAT-5 with those from the sea ice algorithms for the ODIZ.

Algorithm	Statistic					
	R	Bias (%)	SE (%)	RMSE (%)	*Z*	*p*
NT	0.54	4.59	7.09	8.44	−9.98	< 0.001
BT	0.69	10.14	11.93	15.64	−11.37	< 0.001
OSISAF	0.61	5.43	6.28	8.29	−12.31	< 0.001
ASI	0.74	4.37	10.14	11.03	−5.37	< 0.001

Table 7
Comparison of SIC values estimated from KOMPSAT-5 and the sea ice algorithms for the MIZ.

Algorithm	Statistic					
	R	Bias (%)	SE (%)	RMSE (%)	*Z*	*p*
NT	0.65	−5.50	11.88	13.07	−6.76	< 0.001
BT	0.78	17.44	12.43	21.41	−13.66	< 0.001
OSISAF	0.68	−0.63	13.21	13.20	−1.34	0.181
ASI	0.62	11.63	15.49	19.35	−10.36	< 0.001

caused by atmospheric effects over open water. The algorithms using 19 H and 37 H channels, such as the NT and OSISAF algorithms, are more sensitive to atmospheric effects than those using 19 V and 37 V channels, such as the BT frequency mode (Andersen et al., 2006). For the SIC estimation in the ODIZ, the frequency mode is applied for the BT algorithm. However, the BT algorithm overestimated SIC more than other algorithms.

The overestimation of SIC by the algorithms may be a result of inaccuracy of the KOMPSAT-5 ice/water maps. Some drift ice smaller than a grid size of the ice/water maps could be classified as open water (Han et al., 2017) but is already recognized in the PM measurements. Some SIC values from the algorithms were estimated as 0% for low values of KOMPSAT-5 SIC. This was caused by the use of weather filters that can lead to cut-off of low SIC values by reducing the influence of atmospheric water content and wind on the microwave emissivity of ice and water surfaces (Beitsch et al., 2015).

4.2.2. Marginal ice zone

For the MIZ, SIC values estimated from all algorithms were well correlated with those from KOMPSAT-5, with *R* values above 0.6 (Table 7). Meanwhile, statistically significant differences exist between algorithm-derived SIC values, except for OSISAF SIC values, and KOMPSAT-5 SIC values. The OSISAF SIC values showed the smallest bias (−0.63%) and the second smallest value of RMSE (13.20%) compared to the KOMPSAT-5 SIC values (Table 7). The small bias and RMSE of OSISAF SIC values may be due to overestimation of the net ice surface fraction (i.e., SIC excluding melt ponds) by the algorithm (Ivanova et al., 2015), rather than accurate estimations of SICs for the MIZ in summer. Melt ponds are a common feature on the surface of Arctic sea ice during the summer (Perovich et al., 2002; Rösel et al.,

2012; Kim et al., 2013; Han et al., 2016). Fig. 6b and c shows the KOMPSAT-2 pan-sharpened images for the MIZ and the CPIZ, respectively, in the Chukchi Sea on 13 and 15 August 2015. We confirmed from Fig. 6e that many melt ponds formed on the sea ice in the MIZ. The positive anomalies in the June–July mean air temperature at 925 hPa in 2015 over the Chukchi Sea (Fig. 3b) also supported the notion that ice surface melting occurred in the region. As the microwave radiation characteristics of melting ice surfaces are similar to those of open water, this is a significant source of SIC underestimation from most sea ice algorithms for PM measurements (Cavalieri et al., 1990; Comiso and Kwok, 1996; Ivanova et al., 2015; Kern et al., 2016). Meanwhile, the BT frequency mode and Bristol algorithm tend to overestimate the net ice surface fraction owing to elevated T_B values of 37 V for wet snow over ice between melt ponds (Ivanova et al., 2015; Kern et al., 2016).

The NT SIC values showed the smallest RMSE value (13.07%) and were underestimated with a mean bias value of −5.50% (Table 7). The underestimation of SIC occurred more frequently for regions with high SICs (Fig. 8). For regions with lower SICs (SICs ranging from 15% to 40%), the NT SIC values were slightly overestimated, possibly owing to atmospheric water vapor contents. However, the NT SIC values were typically underestimated in regions with higher SICs because of the presence of melt ponds, which are a major source of SIC underestimation by the NT algorithm in summer. Such ponds show a signature similar to that of open water for the NT algorithm (Comiso et al., 1997; Agnew and Howell, 2003; Ivanova et al., 2015; Kern et al., 2016).

SIC values estimated from the BT and ASI algorithms were largely positively biased for the MIZ compared to KOMPSAT-5 SIC values (17.44% and 11.63%, respectively). For the ASI SICs, the overestimation occurred more frequently in regions with lower SICs (Fig. 8). SIC values from the 89 GHz measurements were greatly affected by the atmospheric water content, and were significantly overestimated. This occurred specifically at low ice concentrations due to misinterpretation of open water as sea ice (Spreen et al., 2008; Ivanova et al., 2015). Although the presence of melt ponds leads to the underestimation of SICs by the ASI algorithm (Rösel et al., 2012), the algorithm overestimated the values of SIC.

For the MIZ, the BT algorithm typically applies the frequency mode over seasonal ice zones. The BT frequency mode is less sensitive to atmospheric effects than NT and ASI algorithms, but is more sensitive to melt ponds (Rösel et al., 2012; Ivanova et al., 2014). This can lead to underestimation of SICs in summer. In the Chukchi Sea, however, the BT SIC values showed the largest positive bias and RMSE values (21.41%) compared to the KOMPSAT-5 SIC values.

Melt ponds larger than 125 × 125 m are classified as open water in the KOMPSAT-5 ice/water maps, which can lead to underestimation of KOMPSAT-5 SICs and could be another reason for the positive bias in algorithm-derived SIC values compared to KOMPSAT-5 SIC values. However, the most common melt pond size is < 50 m^2 (Perovich et al., 2002; Mäkynen et al., 2014); therefore, KOMPSAT-5 SIC values should rarely be overestimated.

4.2.3. Consolidated pack ice zone

For the CPIZ, the SIC values estimated by the NT, OSISAF, and ASI algorithms showed statistically significant differences from KOMPSAT-5 SIC values, and were negatively biased (Table 8). Fig. 9 shows an example of a visual comparison between the KOMPSAT-5 ice/water maps, SICs from AARI weekly ice chart and each sea ice algorithm for the CPIZ. The SICs from the ice chart well reflected well the distribution of sea ice observed in the KOMPSAT-5 ice/water maps. However, the SIC values from the algorithms, except for the BT algorithm, seemed to be underestimated compared to those from the ice chart. Based on the fact that strong positive air temperature anomalies were observed in the region (Fig. 3b), the ice surface melting as shown in Fig. 6c could be a reason for the negative biases in SIC estimated by the algorithms in the CPIZ.

Despite the statistically significant difference, the ASI SIC values showed a fairly good correlation with the KOMPSAT-5 SIC values (R value of 0.73) but were slightly underestimated, showing a mean bias value of −8.53% and an RMSE of 10.45%. The largest negative bias and RMSE values of the SICs were estimated by the NT algorithm (−25.65% and 26.72%, respectively). This is possibly owing to ice surface melting in the CPIZ. The OSISAF SIC values showed the second largest value of RMSE (14.84%) and the smallest value of R (0.34). The Bristol algorithm used in the OSISAF algorithm for high SCI is less sensitive to surface emissivity variability in regions with high SICs in winter and it has been reported as an optimum algorithm (Ivanova et al., 2015; Tonboe et al., 2016). However, the sensitivity of the Bristol algorithm to surface effects is greater in summer than in winter because the ice surface is typically more stable in winter than in summer. This might contribute to underestimation of OSISAF SIC values for the CPIZ. The mean bias and SE of the OSISAF SIC values in regions of the Chukchi Sea with high SICs (i.e., the Bristol algorithm-derived values) in summer are similar to those of other regions, with a mean bias of −8.9% and SE of 11.5%, respectively, reported by Andersen et al. (2007). The BT SIC values were slightly overestimated compared to the KOMPSAT-5 SICs (a mean bias value of 1.53%) and had the smallest RMSE (6.27%).

Table 8
Comparison of SIC values estimated from KOMPSAT-5 with those from the sea ice algorithms for the CPIZ.

Algorithm	Statistic					
	R	Bias (%)	SE (%)	RMSE (%)	Z	p
NT	0.52	−25.65	7.54	26.72	−6.03	< 0.001
BT	0.37	1.53	6.10	6.23	−1.60	0.110
OSISAF	0.34	−7.59	12.89	14.84	−2.97	0.003
ASI	0.73	−8.53	6.10	10.45	−5.74	< 0.001

The PM SIC retrieval algorithms typically overestimated SICs for the ODIZ. This suggests that the PM SIC-derived latitudes of the location of the ice edge, defined as the 15% SIC contour (Comiso, 2006; Cavalieri and Parkinson, 2012; Steele and Ermold, 2015), could be geographically lower than the actual locations in the Chukchi Sea in summer. This would result in inaccurate estimation of sea ice extent, defined as the sum of the grid area containing grids with SIC values of at least 15% (Cavalieri and Parkinson, 2012). The erroneous retrieval of SIC values for the MIZ and CPIZ by the algorithms led to inaccurate estimation of summer sea ice area, defined as the sum of the product of the grid area and the SIC value for grids with an SIC value of at least 15% (Cavalieri and Parkinson, 2012). The parameters of sea ice area and extent are primarily used to predict climate change (Vinnikov et al., 1999; Francis et al., 2009; Vihma, 2014), and the differences in sea ice area and extent estimated by the sea ice algorithms predict different trends of climate change. The age of sea ice is typically estimated by tracking each grid cell of PM SIC products with a value of at least 15% from year to year (Maslanik et al., 2011). Therefore, the erroneous SIC retrievals from the algorithms in the Chukchi Sea could lead to inaccurate estimation of the age of sea ice there, especially at the boundary of the MIZ.

4.3. Comparison of biases from PM SICs with NWP data

4.3.1. Comparison of positive biases from PM SICs with NWP data

The relationships between the values of FNR_{OW} and FNR_{SI} from the algorithms and the atmospheric conditions predicted from the ERA Interim reanalysis data were investigated. Fig. 10 shows the correlations of the values of FNR_{OW} from each algorithm, along with the atmospheric conditions in the regions with KOMPSAT-5 SIC lower than 40%. These are where the positive biases observed from the algorithms were predominantly. Correlation analyses were also conducted for the ODIZ, the regions with KOMPSAT-5 SIC higher than 40% and the

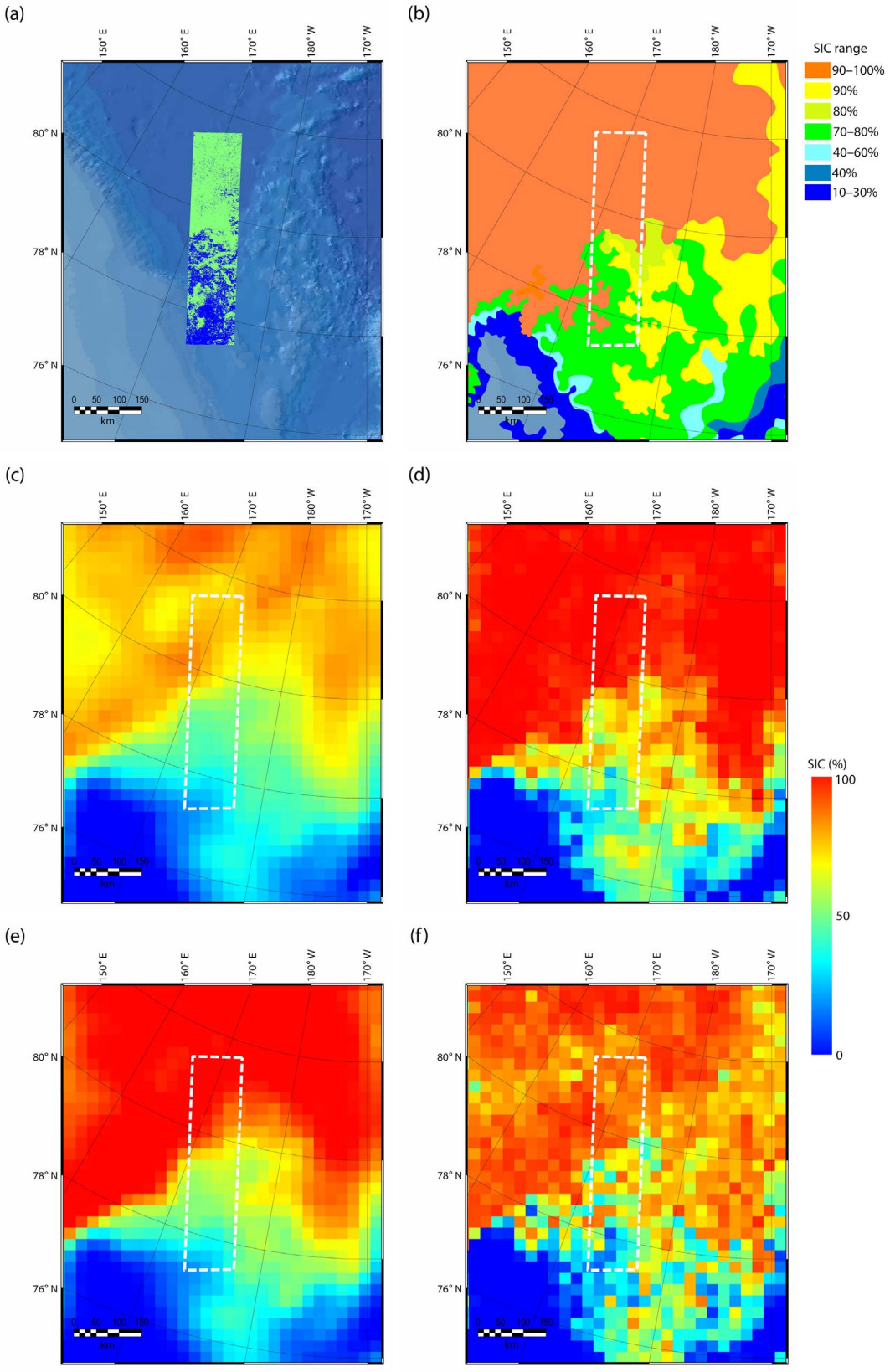

Fig. 9. An example of (a) KOMPSAT-5 ice/water maps for the CPIZ generated from the SAR images obtained on 18 August 2015, (b) SIC from AARI weekly ice charts released on 18 August 2015, (c) SIC products from the NT, (d) BT, (e) OSISAF, and (f) ASI algorithms. The white-dotted box in (b)–(f) correspond to the coverage of the KOMPSAT-5 ice/water maps in (a).

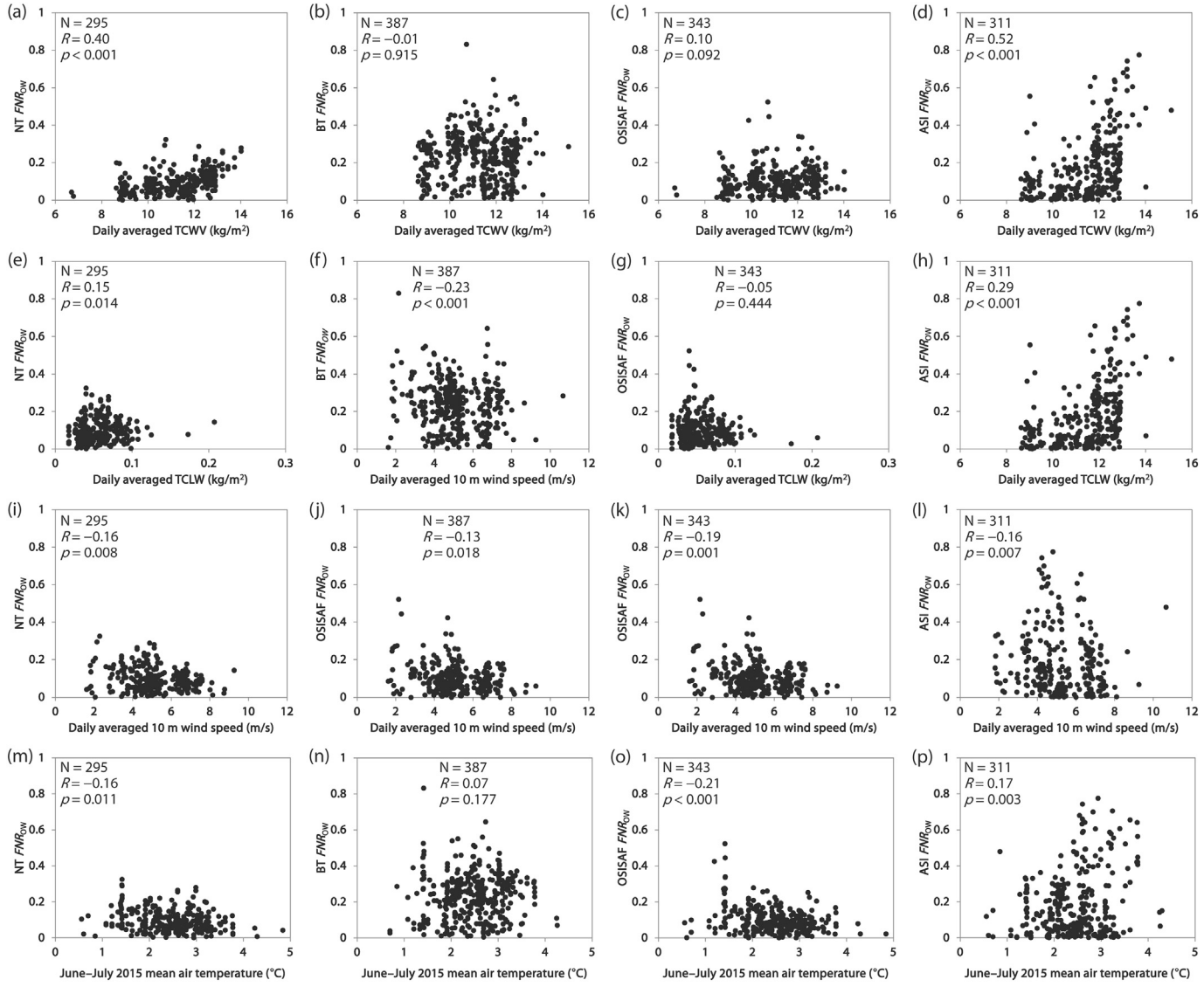

Fig. 10. Correlations of values of FNR_{OW} from the NT, BT, OSISAF, and ASI algorithm with (a)–(d) daily averaged total columnar water vapor (TCWV), (e)–(h) daily averaged total cloud liquid water (TCLW), (i)–(l) daily averaged 10 m wind speed, and (m)–(p) June–July 2015 mean air temperature at 925 hPa level at the regions with KOMPSAT-5 SIC lower than 40%. In each scatter plot, N represents the number of values used for the correlation analysis.

regions with all KOMPSAT-5 SIC values (Table 9). In each scatter plot of Fig. 10 and in Table 9, the *p*-value below 0.05 means that the correlation was statistically significant. As the values of FNR_{OW} and FNR_{SI} were derived from the values of SIC by the KOMPSAT-5 ice/water maps and the sea ice algorithms, which did not follow a normal distribution, the Spearman correlation coefficient (*R*) was computed to assess the strength of relationships between the atmospheric conditions and the biases from the algorithms.

For all SIC ranges, the values of FNR_{OW} from the NT and ASI algorithms showed statistically significant positive correlation with the amount of daily averaged TCWV with the *R* value of 0.39 and 0.38, respectively (Table 9). Such significant positive correlations were slightly stronger at both the regions of with KOMPSAT-5 SIC lower than 40% (0.40 with NT and 0.52 with ASI, Fig. 10a and d) and in the ODIZ (0.43 with NT and 0.46 with ASI, Table 9). This explains that the atmospheric water vapor content contributed to the positive biases of the NT and ASI algorithms. In the regions with KOMPSAT-5 SIC higher than 40%, however, the FNR_{OW} values from the NT and ASI algorithms were not significantly correlated with the TCWV. Meanwhile, the correlations analyzed at the CPIZ for the NT algorithm were unreliable due to insufficient number of SIC values (sample size too low). The required number of SIC values was determined to be > 29 by power analysis for a Spearman correlation conducted in G*Power (Faul et al., 2007) using an effect size of 0.5, an alpha of 0.05 and a power of 0.8.

The increasing trend in values of FNR_{OW} from the ASI algorithm with increasing amount of TCWV was much larger than for the NT algorithm. This indicates that the misinterpretation of open water as sea ice due to the atmospheric water vapor content is more severe in the ASI algorithm than in the NT algorithm. The ASI algorithm using 89 GHz channels is most sensitive to atmospheric water content over open water (Spreen et al., 2008; Ivanova et al., 2015). Moreover, the weather filters using the channels with lower spatial resolution than 89 GHz channels might be missed at pixels of ASI SIC along the ice edge, which could be another source of the positive bias of the ASI algorithm in low SIC regions (Spreen et al., 2008).

The *R* values between the values of FNR_{OW} from the BT and OSISAF algorithms, and the daily averaged TCWV, were not statistically significant (*p*-values > 0.05), except for the regions with KOMPSAT-5 SIC higher than 40% (Table 9). The effects of the water vapor content on the positive bias from the algorithms for the low SIC regions could not be analyzed. For the regions with KOMPSAT-5 SIC higher than 40%, the values of FNR_{OW} from the BT and OSISAF algorithms were significantly

Table 9
Correlations of FNR_{OW} from the algorithms with atmospheric conditions from the ERA Interim reanalysis at ODIZ, the regions with KOMPSAT-5 (K5) SIC higher than 40% and the regions with all K5 SIC values. N represents the number of values used for the correlation analysis.

Algorithm	Statistic								
	ODIZ			Regions with K5 SIC higher than 40%			Regions with all K5 SIC values		
	N	*R*	*p*	N	*R*	*p*	N	*R*	*p*
Correlation of FNR_{OW} with daily averaged TCWV									
NT	216	0.43	< 0.001	9	0.17	0.668	304	0.39	< 0.001
BT	218	0.01	0.914	114	−0.39	< 0.001	501	−0.06	0.222
OSISAF	249	0.10	0.166	51	−0.38	0.014	394	0.02	0.760
ASI	172	0.46	< 0.001	61	−0.03	0.806	372	0.38	< 0.001
Correlation of FNR_{OW} with daily averaged total TCLW									
NT	216	0.14	0.054	9	0.03	0.932	304	0.16	0.010
BT	218	−0.24	0.001	114	−0.57	< 0.001	501	−0.26	< 0.001
OSISAF	249	−0.08	0.291	51	−0.57	< 0.001	394	−0.09	0.017
ASI	172	0.27	0.001	61	−0.07	0.568	372	0.23	< 0.001
Correlation of FNR_{OW} with daily averaged 10 m wind speed									
NT	216	−0.15	0.035	9	−0.07	0.865	304	−0.14	0.022
BT	218	−0.01	0.847	114	−0.48	< 0.001	501	−0.22	< 0.001
OSISAF	249	−0.16	0.028	51	−0.41	< 0.001	394	−0.28	< 0.001
ASI	172	−0.12	0.153	61	0.03	0.845	372	−0.20	< 0.001
Correlation of FNR_{OW} with June–July mean air temperature at 925 hPa									
NT	216	−0.05	0.471	9	0.13	0.731	304	−0.12	0.045
BT	218	0.11	0.142	114	−0.53	< 0.001	501	0.07	0.133
OSISAF	249	−0.10	0.181	51	−0.68	< 0.001	394	−0.28	< 0.001
ASI	172	0.19	0.013	61	−0.02	0.889	372	0.08	0.137

negatively correlated with the amount of TCWV, with *R* values of −0.39 and −0.38, respectively (Table 9). The algorithms were strongly negatively correlated with the June–July mean air temperature at 925 hPa (*R* value of −0.53 and −0.68, respectively, Table 9), which suggests that overestimation of SIC by the algorithms might be compensated by decreased T_B due to ice surface melting. These results could be due to the lower sensitivity of algorithms to water vapor content over sea ice, but more sensitive to ice surface melting than in other algorithms (Rösel et al., 2012; Ivanova et al., 2014).

For all SIC ranges, the values of FNR_{OW} from the NT and ASI algorithms shows statistically significant, but weak positive correlations with the daily averaged TCLW with the *R* value of 0.16 and 0.23, respectively (Table 9). Meanwhile, statistically significant negative correlations were observed between the values of FNR_{OW} from the BT algorithm and the TCLW, and the values of FNR_{OW} from the OSISAF algorithm and the TCLW (Table 9). The FNR_{OW} from all algorithms and the daily averaged wind speed at 10 m also showed significantly negative correlations (Fig. 10i to l, Table 9). These are contrary to the expectation that the misinterpretation of open water to sea ice is greater with increasing wind speed and amount of cloud liquid water. Both the weak correlations and the negative correlations can be attributed to temporally rapid variations of atmospheric conditions during a day (Cavalieri et al., 1995). Fig. 11 shows a boxplot of the coefficient of variation (CV) of the daily TCWV, TCLW and 10 m wind speed predicted from the ERA Interim reanalysis data for the locations and dates of the PM SICs. While most of the values of the CV for TCWV were below 0.1, with a mean value of 0.06, the TCLW and 10 m wind speed showed large variations in a day (mean value of CV of 0.29 and 0.22, respectively). This was probably due to continuous changes in the winds and movements of clouds. Therefore, the values of the daily averaged TCLW and 10 m wind speed are considered unreliable and difficult to use for finding reasonable correlations with the values of FNR_{OW} and FNR_{SI} from the algorithms.

The correlations of values of FNR_{OW} from the algorithms and the June–July mean air temperature at 925 hPa were not significant for the ODIZ. They were very weak for other regions, even if they were significant, except for the regions with KOMPSAT-5 SIC higher than 40% for the BT and OSISAF algorithm. This could be because overestimation

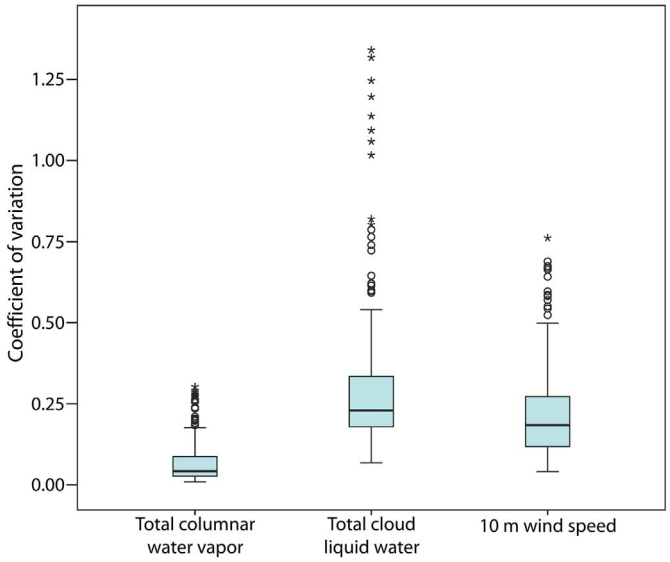

Fig. 11. Boxplots of the coefficient of variation for daily total columnar water vapor, daily total cloud liquid water, and daily 10 m wind speed predicted from the ERA Interim reanalysis data. Colored boxes represent the interquartile range of the samples, and a line inside the box indicates the median value of the samples. The vertical lines above and below the box represent 1.5-times the interquartile range beyond the lower and upper quartiles. The circles and asterisks represent the outliers (samples between 1.5 and 3 interquartile ranges from the box) and extreme outliers (samples > 3 interquartile ranges from the box), respectively. (For interpretation of the references to color in this figure legend, the reader is referred to the web version of this article.)

by the algorithms of the low SIC regions might be more sensitive to other atmospheric effects such as atmospheric water vapor. This makes it difficult to interpret the relationship between the FNR_{OW} and the mean air temperature in such regions.

We could not find the influences of the atmospheric effects on the positive biases for low SIC regions from the BT and OSISAF algorithms. A possible reason for the positive bias from the BT algorithm is that the tie points of open water in Arctic seasonal ice zones might result in

significantly erroneous SIC values in summer, even though they were defined by regions and modified as time passed (Comiso, 1995; Ivanova et al., 2015). The positive biases in low SIC regions from the OSISAF algorithm may be because the atmospheric effect induced noise in T_B over open water might not be well corrected by NWP data (Tonboe et al., 2016). By correlation analyses, we found that the SIC values from the NT and ASI algorithm in the low SIC regions were caused by the atmospheric water vapor content. The Chukchi Sea is the one of the regions in the Arctic where the amount of atmospheric water vapor content in summer and early autumn has increased dramatically. This trend exceeds 1.5 mm per decade (Serreze et al., 2012). This increasing water vapor content was predominantly observed over open water. This means that the SIC values from the sea ice algorithms could have more positive bias in low SIC regions in the Chukchi Sea than in other regions of the Arctic in summer, due to the atmospheric water vapor content.

The positive bias of SIC estimated by the NT, BT, and OSISAF algorithms in low SIC regions may also be due to different footprint sizes of the 19 GHz and 37 GHz channels (Table 1), which affect SIC estimation in the algorithms (Ivanova et al., 2014). Moreover, the footprint sizes larger than the grid size in the SIC products can include T_B information from the ice pack, which could be another source of SIC overestimation at the ice edge (Meier, 2005). The footprint size of the 89 GHz channels of AMSR2 is sufficient (3 × 5 km) (Table 2) and should not have an influence on the positive bias of ASI SIC values. The overestimation of SIC values by the ASI algorithm for low SIC regions could be mainly due to misinterpretation of open water as sea ice in the 89 GHz measurements (Spreen et al., 2008; Ivanova et al., 2015).

4.3.2. Comparison of negative biases from PM SICs with NWP data

Fig. 12 shows the relationships between the values of FNR_{SI} from the algorithms and the June–July 2015 mean air temperature at 925 hPa level, and the FNR_{SI} from the algorithms and the daily averaged TCWV at the regions with KOMPSAT-5 SIC higher than 40% where the positive biases from the algorithm were predominantly observed. The correlations for the regions with KOMPSAT-5 SIC lower than 40%, KOMPSAT-5 SIC from 40% to 80% (i.e., the regions where positive biases were predominantly observed in MIZ) and CPIZ are listed in Table 10. The analyses of the relationships between the values of FNR_{SI} and daily averaged TCLW, and the values of FNR_{SI} and daily averaged 10 m wind speed were not performed due to large variability in the atmospheric conditions over a day (Fig. 11). In the regions with KOMPSAT-5 SIC lower than 40%, the results from all the algorithms were not significantly correlated with the mean air temperature (Table 10) because other atmospheric influences had greater effects on the values of SIC from the algorithm in the low SIC regions.

In the regions with KOMPSAT-5 SIC higher than 40%, strong positive correlations were observed between the values of FNR_{SI} from the NT and OSISAF algorithm, with the June–July 2015 mean air temperature at 925 hPa (R value of 0.50 with NT and 0.55 with OSISAF) (Fig. 12a and c). The values of FNR_{SI} from the algorithms computed for the regions with KOMPSAT-5 SIC of 40%–80%, and in CPIZ, were also strongly, positively correlated with the June–July mean air temperature (R values ranging from 0.43 to 0.58). This supports the notion that the underestimation of SIC from the algorithms in MIZ and CPIZ was due to variability in the surface emissivity caused by ice surface melting and the presence of melt ponds (Andersen et al., 2007; Ivanova et al., 2015). For the CPIZ, the largest negative bias (−25.65%) and RMSE (26.72%) values were estimated by the NT algorithm (Table 8). The bias of the NT SICs in Baffin Bay, Barents Sea, Beaufort Sea, Lincoln Sea, and Greenland Sea with high SICs has been reported as approximately −15% in summer (Andersen et al., 2007; Meier, 2005). This is much smaller than that for the Chukchi Sea in this study. Unfortunately, we cannot confirm the exact surface conditions of the sea ice investigated in the previous research. However, it is known that sea ice melting in the Chukchi Sea in summer can be more serious than in other regions owing to the oceanic heat flux transportation from the Pacific Ocean, warm southerly winds and increasing water vapor content (Serreze et al., 2012; Stroeve et al., 2012; Serreze et al., 2016). Therefore, the worse performance of SIC retrieval from the NT algorithm in regions of high in the Chukchi Sea in summer was probably because of more severe ice surface melting there. The Bristol algorithm used in the OSISAF algorithm for high SCI regions is less sensitive to surface emissivity variability in winter and has been reported as an optimum algorithm (Ivanova et al., 2015; Tonboe et al., 2016). However, the sensitivity of the Bristol algorithm to variability in the surface emissivity is greater in summer than in winter because the ice surface is typically more stable in winter than in summer. This might contribute to underestimation of OSISAF SIC values for the CPIZ. However, the correlation analysis for the OSISAF algorithm at CPIZ could be unreliable because the number of SIC values used was insufficient.

The BT SIC showed the largest positive biases (Fig. 8). Only a few values of SIC from the BT algorithm were underestimated in the regions with KOMPSAT-5 SIC higher than 40%, of which the values of FNR_{SI} did not show a statistically significant correlation with the June–July mean

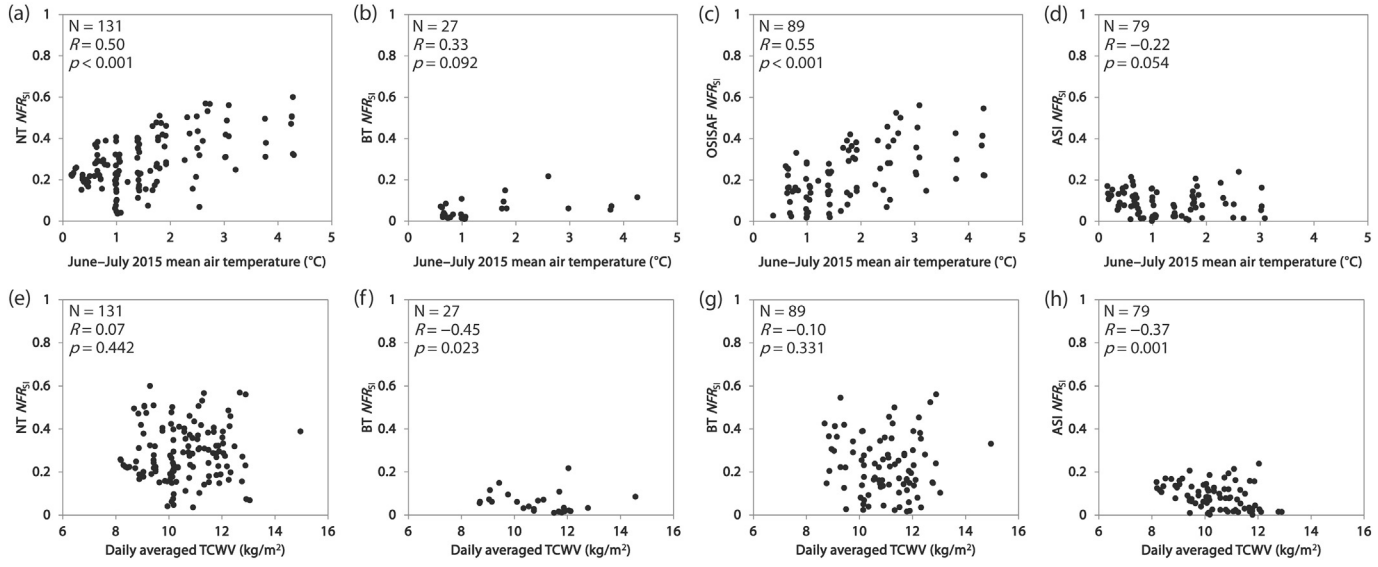

Fig. 12. Correlations of values of FNR_{SI} from the NT, BT, OSISAF, and ASI algorithm with (a)–(d) June–July 2015 mean air temperature at 925 hPa level and (e)–(h) daily averaged total columnar water vapor (TCWV) at the regions with KOMPSAT-5 SIC higher than 40%. In each scatter plot, N represents the number of values used for the correlation analysis.

Table 10
Correlations of FNR_{OW} from the algorithms with atmospheric conditions from the ERA Interim reanalysis data in the regions with KOMPSAT-5 (K5) SIC lower than 40%, the regions with K5 SIC from 40% to 80%, and the CPIZ. N represents the number of values used for the correlation analysis.

Algorithm	Statistic								
	Regions with K5 SIC lower than 40%			Regions with K5 SIC from 40% to 80%			CPIZ		
	N	*R*	*p*	N	*R*	*p*	N	*R*	*p*
Correlation of FNR_{SI} with June–July mean air temperature at 925 hPa									
NT	196	0.01	0.905	83	0.58	< 0.001	48	0.50	< 0.001
BT	103	0.02	0.915	8	0.38	0.352	19	0.89	0.092
OSISAF	148	−0.07	0.510	63	0.53	< 0.001	26	0.43	0.027
ASI	180	−0.01	0.906	33	0.08	0.677	46	−0.34	0.020
Correlation of FNR_{SI} with daily averaged TCWV									
NT	196	−0.14	0.142	83	−0.06	0.620	48	0.25	0.090
BT	103	−0.24	0.268	8	0.17	0.693	19	−0.51	0.023
OSISAF	148	−0.19	0.073	63	−0.05	0.675	26	−0.18	0.393
ASI	180	−0.28	0.009	33	−0.17	0.357	46	−0.48	0.002

air temperature (Fig. 12b and Table 10). This result might be unreliable due to insufficient number of values used in the analysis. A possible reason that the BT algorithm showed the largest overestimation of SICs is that the tie points of sea ice and open water in Arctic seasonal ice zones from August–September used in the algorithm might estimate significantly different regional SIC values. This may be due to regional variation in the atmospheric and surface effects on PM measurements. The values of FNR_{SI} from the ASI algorithm and the June–July 2015 mean air temperature did not show a significant correlation, except when considering the CPIZ only (Fig. 12d and Table 10). Surprisingly, the values of FNR_{SI} from the ASI algorithm in CPIZ showed a statistically significant negative correlation with the June–July 2015 mean air temperature at 925 hPa level (*R* values of −0.34).

We compared the values of FNR_{SI} from the algorithms with the daily averaged total columnar water vapor. The correlations of the values of FNR_{SI} from the OSISAF algorithm with the daily averaged TCWV were not statistically significant regardless of the ranges of SIC values (Fig. 12g and Table 10). Meanwhile, the values of FNR_{SI} from the BT and ASI algorithms were significantly negatively correlated with the TCWV in the regions with KOMPSAT-5 SIC higher than 40% (*R* values of −0.45 with BT and −0.37 with ASI). Such significant negative correlation became stronger for the CPIZ (*R* values of −0.51 with BT and −0.48 with ASI). This might argue that underestimation of ASI SIC in high SIC regions could be strongly compensated by the misinterpretation of open water for sea ice owing to the water vapor content. However, this is contrary to the claims of previous researches that, in regions with high SIC, the atmospheric effects on SIC estimation by the ASI algorithm is less than in regions with low SICs (Spreen et al., 2008; Ivanova et al., 2015). For the BT algorithm, however, the correlation might be unreliable due to the small sample size, as stated above. Nevertheless, considering the statistically significant correlation, the underestimation of BT SIC in high SIC regions may be compensated by the water vapor content, as for the ASI algorithm.

4.3.3. Comparison of differences in PM SICs with NWP data

The differences in SIC values from the algorithms would be due to different sensitivities to atmospheric effects and to ice surface melting. Table 11 shows the correlation of the values of standard deviation (SD) of SIC values from each algorithm with the daily averaged TCWV and the June–July 2015 mean air temperature at the 925 hPa pressure level. The daily averaged TCLW and 10 m wind speed were not considered because of the large temporal variation during a day. For the ODIZ, the SD values and the daily averaged TCWV showed a statistically significant positive *R* value (0.12), but the SD values were not significantly correlated with the mean air temperature (Table 11). The low *R* value between the SD values and the daily averaged TCWV at ODIZ would be because other atmospheric effects such as wind speed and cloud liquid water might affect differences in the PM SICs as well. At both MIZ and CPIZ, the SD values were strongly positively correlated with the June–July 2015 mean air temperature (*R* value of 0.38 and 0.36, respectively) but not significantly correlated with the daily averaged TCWV (Table 11).

Table 11
Correlation of the standard deviation (SD) of SIC from all algorithms with the atmospheric conditions from the ERA Interim reanalysis data.

Regions	Correlation of SD of PM SICs with daily averaged TCWV		Correlation of SD of PM SICs with June–July mean air temperature at 925 hPa	
	Statistic			
	R	*p*	*R*	*p*
ODIZ	0.12	0.032	0.06	0.239
MIZ	0.05	0.483	0.38	< 0.001
CPIZ	−0.09	0.553	0.36	0.012
All SIC ranges	0.04	0.303	−0.05	0.202

When the SIC regions were separated into two regions, where the positive and negative bias from the algorithms was predominantly observed using a threshold of KOMPSAT-5 SIC of 40%, the SD values from the algorithms were significantly positively correlated with the daily averaged TCWV for the lower SIC regions (*R* value of 0.14) and with the mean air temperature at the higher SIC regions (*R* value of 0.41) (Fig. 13). The SD values were not significantly correlated with the daily averaged TCWV at the higher SIC regions and the mean air temperature at the lower SIC regions, respectively. These results support the idea that the differences in SIC values from the algorithms are attributable to different sensitivities to atmospheric water vapor content in the low SIC regions and to ice surface melting in high SIC regions.

The differences between the SICs for the Chukchi Sea derived from the sea ice algorithms and KOMPSAT-5 ice/water maps were analyzed for the summer season. This provided invaluable findings about the performance of different sea ice algorithms for the Chukchi Sea in summer according to the range of SIC. However, the factors influencing the SIC values of the algorithms, such as ice type, ice thickness, snow properties, and melt pond fraction, cannot be analyzed together due to the lack of in situ data, which is a limitation of this research. If sufficient in situ data of sea ice physical properties were obtained, a more accurate analysis of SIC estimation errors from sea ice algorithms implemented for PM measurements would be possible.

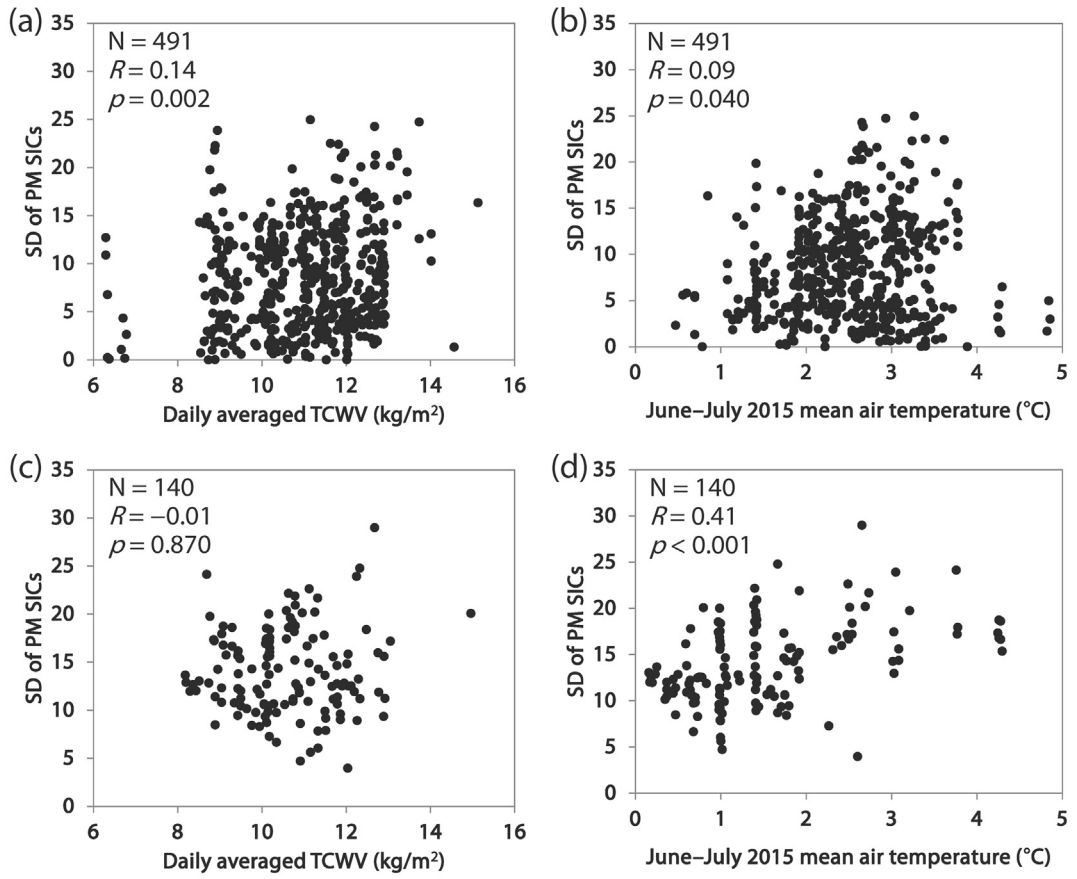

Fig. 13. Correlations of SD values of SIC from the NT, BT, OSISAF, and ASI algorithm with daily averaged total columnar water vapor (TCWV) and the June–July 2015 mean air temperature at 925 hPa level (a and b) at the regions with KOMPSAT-5 SIC lower than 40% and (c and d) the regions with KOMPSAT-5 SIC higher than 40%, respectively. In each scatter plot, N represents the number of values used for the correlation analysis.

5. Conclusion

We evaluated values of the sea ice concentration (SIC) estimated by the NT, BT, OSISAF, and ASI algorithms for the Chukchi Sea in summer using KOMPSAT-5 SAR images obtained in EW mode, along with numerical weather prediction data from the ERA Interim reanalysis. Ice/water maps were generated using the binary classification of texture features in the SAR images based on the Random Forest learning approach, which were accurate enough to calculate SIC values for evaluation of sea ice algorithm-derived SIC values. The SIC values estimated by the algorithms showed a good correlation with those from KOMPSAT-5 ice/water maps, but had RMSE values over 10%. Considering all SIC ranges, the OSISAF and ASI algorithms slightly overestimated SIC values, but NT and BT algorithms largely underestimated and overestimated SIC values, respectively. The SIC values estimated by the algorithms showed different error trends for different ranges of SIC. For the ODIZ, where the range of SICs was 0% to 15%, all algorithms largely underestimated SIC values compared to the KOMPSAT-5 SIC values. The OSISAF SIC values were slightly biased compared to those from KOMPSAT-5 ice/water maps for the MIZ, where the SIC values ranged from 15% to 80%, but showed large RMSE values. SIC values estimated for the MIZ by three other algorithms showed high bias and RMSE compared to KOMPSAT-5 SIC. The NT algorithm largely underestimated SIC, and the BT and ASI algorithms greatly overestimated it. All sea ice algorithms, except the BT algorithm, typically underestimated SIC values for the CPIZ where SICs exceeded 80%. The positive bias from the NT and ASI algorithms was influenced by atmospheric water vapor content, while the negative bias from the NT and OSISAF algorithms was due to ice surface melting. The underestimates of SIC by the BT and ASI algorithms in high SIC regions might be compensated by the effect of the atmospheric water vapor content. Errors in the SIC values estimated by the algorithms would lead to inaccurate estimation of ice edge location, sea ice area, and sea ice extent in the Chukchi Sea in summer using PM SIC products. The differences in SIC values estimated by the algorithms are likely caused by different sensitivities to atmospheric water vapor content in low SIC regions and to ice surface melting in high SIC regions.

This study statistically and quantitatively evaluated PM SIC products for the Chukchi Sea in summer using accurate ice/water maps generated from KOMPSAT-5 SAR images. However, factors affecting SIC estimation by the sea ice algorithms, such as ice type, ice thickness, surface properties, melt pond fractions, and atmospheric water content, were not considered. Field observations to provide such factors could help evaluate the sea ice algorithms more accurately. In future research, we will obtain various in situ data of sea ice and atmospheric characteristics from the annual summer Arctic expedition of ARAON. This will enable a more accurate evaluation of SICs estimated from various SIC retrieval algorithms using PM measurements, and allow us to investigate the influence of ice and atmospheric properties on errors in the PM SIC products.

Acknowledgements

This research was supported by the Korea Polar Research Institute (KOPRI) Grant PE18120 (Research on analytical technique for satellite observation of Arctic sea ice). This research is based on the synergy between KOPRI and the Korea Aerospace Research Institute (KARI). The National Satellite Operation & Application Center at the KARI provided both KOMPSAT-5 and KOMPSAT-2 data for this research.

References

Agnew, T., Howell, S., 2003. The use of operational ice charts for evaluating passive microwave ice concentration data. Atmosphere-Ocean 41 (4), 317–331.

Andersen, S., Tonboe, R., Kern, S., Schyberg, H., 2006. Improved retrieval of sea ice total concentration from spaceborne passive microwave observations using numerical weather prediction model fields: an intercomparison of nine algorithms. Remote Sens. Environ. 104, 374–392.

Andersen, S., Tonboe, R., Kaleschke, L., Heygster, G., Pedersen, L.T., 2007. Intercomparison of passive microwave sea ice concentration retrievals over the high-concentration Arctic sea ice. J. Geophys. Res. 112, C08004. http://dx.doi.org/10.1029/2006JC003543.

Arrigo, K.R., van Dijken, G., Pabi, S., 2008. Impact of a shrinking Arctic ice cover on marine primary production. Geophys. Res. Lett. 35, L19603. http://dx.doi.org/10.1029/2008GL035028.

Beitsch, A., Kern, S., Kaleschke, L., 2015. Comparison of SSM/I and AMSR-E sea ice concentrations with ASPeCt ship observations around Antarctica. IEEE Trans. Geosci. Remote Sens. 53 (4), 1985–1996.

Belchansky, G.I., Douglas, D.C., 2002. Seasonal comparisons of sea ice concentration estimates derived from SSM/I, OKEAN, and RADARSAT data. Remote Sens. Environ. 81 (1), 67–81.

Breiman, L., 2001. Random forests. Mach. Learn. 45 (1), 5–32.

Breivik, L.-A., Eastwood, S., Godøy, Ø., Schyberg, H., Andersen, S., Tonboe, R., 2001. Sea ice products for EUMETSAT satellite application facility. Can. J. Remote. Sens. 27 (5), 403–410.

Cavalieri, D.J., Parkinson, C.L., 2012. Arctic sea ice variability and trends, 1979–2010. Cryosphere 6, 881–889.

Cavalieri, D.J., Gloersen, P., Campbell, W.J., 1984. Determination of sea ice parameters with the Nimbus 7 SMMR. J. Geophys. Res. 89 (D4), 5355–5369. http://dx.doi.org/10.1029/JD089iD04p05355.

Cavalieri, D.J., Burns, B.A., Onstott, R.G., 1990. Investigation of the effects of summer melt on the calculation of sea ice concentration using active and passive microwave data. J. Geophys. Res. 95 (C4), 5359–5369. http://dx.doi.org/10.1029/JC095iC04p05359.

Cavalieri, D.J., Germain, K.M.S., Swift, C.T., 1995. Reduction of weather effects in the calculation of sea-ice concentration with the DMSP SSM/I. J. Glaciol. 41 (139), 455–464.

Cavalieri, D.J., Parkinson, C.L., Vinnikov, K.Y., 2003. 30-year satellite record reveals contrasting Arctic and Antarctic decadal sea ice variability. Geophys. Res. Lett. 30 (1970). http://dx.doi.org/10.1029/2003GL018031.

Cavalieri, D.J., Markus, T., Hall, D.K., Gasiewski, A.J., Klein, M., Ivanoff, A., 2006. Assessment of EOS Aqua AMSR-E Arctic sea ice concentrations using Landsat-7 and airborne microwave imagery. IEEE Trans. Geosci. Remote Sens. 44 (11), 3057–3069.

Cavalieri, D.J., Markus, T., Hall, D.K., Ivanoff, A., Glick, E., 2010. Assessment of AMSR-E Antarctic winter sea-ice concentrations using Aqua MODIS. IEEE Trans. Geosci. Remote Sens. 48 (9), 3331–3339.

Clausi, D.A., 2001. Comparison and fusion of co-occurrence, Gabor and MRF texture features for classification of SAR sea-ice imagery. Atmosphere-Ocean 39 (3), 183–194.

Clausi, D.A., 2002. An analysis of co-occurrence texture statistics as a function of grey level quantization. Can. J. Remote. Sens. 28 (1), 45–62.

Comiso, J.C., 1986. Characteristics of Arctic winter sea ice from satellite multispectral microwave observations. J. Geophys. Res. 91 (C1), 975–994. http://dx.doi.org/10.1029/JC091iC01p00975.

Comiso, J.C., 1995. SSM/I sea ice concentrations using bootstrap algorithm. In: NASA Reference Publication 1380.

Comiso, J.C., 2006. Abrupt decline in the Arctic winter sea ice cover. Geophys. Res. Lett. 33, L18504. http://dx.doi.org/10.1029/2006GL027341.

Comiso, J.C., 2012. Large decadal decline of the Arctic multiyear ice cover. J. Clim. 25, 1176–1193.

Comiso, J.C., Kwok, R., 1996. Surface and radiative characteristics of the summer Arctic sea ice cover from multisensor satellite observations. J. Geophys. Res. 101 (C12), 28397–28416. http://dx.doi.org/10.1029/96JC02816.

Comiso, J.C., Cavalieri, D.J., Parkinson, C.L., Gloersen, P., 1997. Passive microwave algorithms for sea ice concentration: a comparison of two techniques. Remote Sens. Environ. 60, 357–384.

Comiso, J.C., Cavalieri, D.J., Markus, T., 2003. Sea ice concentration, ice temperature, and snow depth using AMSR-E data. IEEE Trans. Geosci. Remote Sens. 41 (2), 243–252.

Comiso, J.C., Parkinson, C.L., Gersten, R., Stock, L., 2008. Accelerated decline in the Arctic sea ice cover. Geophys. Res. Lett. 35, L01703. http://dx.doi.org/10.1029/2007GL031972.

Cracknell, M.J., Reading, A.M., 2014. Geological mapping using remote sensing data: a comparison of five machine learning algorithms, their response to variations in the spatial distribution of training data and the use of explicit spatial information. Comput. Geosci. 63, 22–33.

Cuzzone, J., Vavrus, S., 2011. The relationships between Arctic sea ice and cloud-related variables in the ERA-Interim reanalysis and CCSM3. Environ. Res. Lett. 6 (1), 014016.

Dabboor, M., Geldsetzer, T., 2014. Towards sea ice classification using simulated RADARSAT Constellation Mission compact polarimetric SAR imagery. Remote Sens. Environ. 140, 189–195.

Dee, D.P., Uppala, S.M., Simmons, A.J., Berrisford, P., Poli, P., Kobayashi, S., Andrae, U., Balmaseda, M.A., Balsamo, G., Bauer, P., Bechtold, P., Beljaars, A.C.M., van de Berg, L., Bidlot, J., Bormann, N., Delsol, C., Dragani, R., Fuentes, M., Geer, A.J., Haimberger, L., Healy, S.B., Hersbach, H., H'olm, E.V., Isaksen, L., Kållberg, P., Köhler, M., Matricardi, M., McNally, A.P., Monge-Sanz, B.M., Morcrette, J.-J., Park, B.-K., Peubey, C., de Rosnay, P., Tavolato, C., Thépaut, J.-N., Vitart, F., 2011. The ERA-Interim reanalysis: configuration and performance of the data assimilation system. Q. J. R. Meteorol. Soc. 137, 553–597.

Faul, F., Erdfelder, E., Lang, A.G., Buchner, A., 2007. G* Power 3: a flexible statistical power analysis program for the social, behavioral, and biomedical sciences. Behav. Res. Methods 39 (2), 175–191.

Francis, J.A., Chan, W., Leathers, D.J., Miller, J.R., Veron, D.E., 2009. Winter Northern Hemisphere weather patterns remember summer Arctic sea-ice extent. Geophys. Res. Lett. 36, L07503. http://dx.doi.org/10.1029/2009GL037274.

Gloersen, P., Cavalieri, D.J., 1986. Reduction of weather effects in the calculation of sea ice concentration from microwave radiances. J. Geophys. Res. 91 (C3), 3913–3919. http://dx.doi.org/10.1029/JC091iC03p03913.

Grebmeier, J.M., Moore, S.E., Overland, J.E., Frey, K.E., Gradinger, R., 2010. Biological response to recent Pacific Arctic sea ice retreats. Eos 91 (18), 161–162.

Han, H., Lee, S., Im, J., Kim, M., Lee, M.I., Ahn, M.H., Chung, S.R., 2015. Detection of convective initiation using Meteorological Imager onboard Communication, Ocean, and Meteorological Satellite based on machine learning approaches. Remote Sens. 7, 9184–9204.

Han, H., Im, J., Kim, M., Sim, S., Kim, J., Kim, D.-j, Kang, S.H., 2016. Retrieval of melt ponds on arctic multiyear sea ice in summer from TerraSAR-x dual-polarization data using machine learning approaches: a case study in the Chukchi Sea with mid-incidence angle data. Remote Sens. 8, 57.

Han, H., Hong, S.-H., Kim, H.-c, Chae, T.-B., Choi, H.J., 2017. A study of the feasibility of using KOMPSAT-5 SAR data to map sea ice in the Chukchi Sea in late summer. Remote Sens. Lett. 8 (5), 468–477.

Haralick, R.M., Shanmugam, K., Dinstein, I., 1973. Textural features for image classification. IEEE Trans. Syst. Man Cybern. SMC-3 (6), 610–621.

Hayes, M.M., Miller, S.N., Murphy, M.A., 2014. High-resolution landcover classification using Random Forest. Remote Sens. Lett. 5 (2), 112–121.

Heinrichs, J.F., Cavalieri, D.J., Markus, T., 2006. Assessment of the AMSR-E Sea Ice-Concentration product at the ice edge using RADARSAT-1 and MODIS imagery. IEEE Trans. Geosci. Remote Sens. 44 (11), 3070–3080.

Ho, J., 2010. The implications of Arctic sea ice decline on shipping. Mar. Policy 34 (3), 713–715.

Holland, M.M., Bitz, C.M., Tremblay, B., 2006. Future abrupt reductions in the summer Arctic sea ice. Geophys. Res. Lett. 33, L23503. http://dx.doi.org/10.1029/2006GL028024.

Imaoka, K., Kachi, M., Fujii, H., Murakami, H., Hori, M., Ono, A., Igarashi, T., Nakagawa, K., Oki, T., Honda, Y., Shimoda, H., 2010. Global Change Observation Mission (GCOM) for monitoring carbon, water cycles, and climate change. Proc. IEEE 98 (5), 717–734.

Immitzer, M., Vuolo, F., Atzberger, C., 2016. First experience with Sentinel-2 data for crop and tree species classifications in central Europe. Remote Sens. 8 (3), 166.

Inoue, J., Yamazaki, A., Ono, J., Dethloff, K., Maturilli, M., Neuber, R., Edwards, P., Yamaguchi, H., 2015. Additional Arctic observations improve weather and sea-ice forecasts for the Northern Sea Route. Sci. Rep. 5, 16868. http://dx.doi.org/10.1038/srep16868.

Ivanova, N., Johannessen, O.M., Pedersen, L.T., Tonboe, R.T., 2014. Retrieval of Arctic sea ice parameters by satellite passive microwave sensors: a comparison of eleven sea ice concentration algorithms. IEEE Trans. Geosci. Remote Sens. 52 (11), 7233–7246.

Ivanova, N., Pedersen, L.T., Tonboe, R.T., Kern, S., Heygster, G., Lavergne, T., Sørensen, A., Saldo, R., Dybkjær, G., Brucker, L., Shokr, M., 2015. Inter-comparison and evaluation of sea ice algorithms: towards further identification of challenges and optimal approach using passive microwave observations. Cryosphere 9, 1797–1817.

Johannessen, O.M., Bengtsson, L., Miles, M.W., Kuzmina, S.I., Semenov, V.A., Alekseev, G.V., Nagurnyi, A.P., Zakharov, V.F., Bobylev, L.P., Pettersson, L.H., Hasselmann, K., Cattle, H.P., 2004. Arctic climate change: observed and modelled temperature and sea-ice variability. Tellus A 56 (4), 328–341.

Kay, J.E., Holland, M.M., Jahn, A., 2011. Inter-annual to multi-decadal Arctic sea ice extent trends in a warming world. Geophys. Res. Lett. 38, L15708. http://dx.doi.org/10.1029/2011GL048008.

Kern, S., Rösel, A., Pedersen, L.T., Ivanova, N., Saldo, R., Tonboe, R.T., 2016. The impact of melt ponds on summertime microwave brightness temperatures and sea-ice concentrations. Cryosphere 10, 2217–2239.

Khon, V.C., Mokhov, I.I., Latif, M., Semenov, V.A., Park, W., 2010. Perspectives of Northern Sea Route and Northwest Passage in the twenty-first century. Clim. Chang. 100, 757–768.

Kim, D.-j, Hwang, B., Chung, K.H., Lee, S.H., Jung, H.-S., Moon, W.M., 2013. Melt pond mapping with high-resolution SAR: the first view. Proc. IEEE 101 (3), 748–758.

Kim, Y., Ji, Y., Han, H., Lee, J., Lee, H., 2014. Analysis of sea route to the Jangbogo Antarctic Research Station by using passive microwave sea ice concentration data. Korean J. Remote Sens. 30 (5), 677–686.

Kim, Y.H., Im, J., Ha, H.K., Choi, J.K., Ha, S., 2014. Machine learning approaches to coastal water quality monitoring using GOCI satellite data. GISci. Remote Sens. 51 (2), 158–174.

Kim, M., Im, J., Han, H., Kim, J., Lee, S., Shin, M., Kim, H.-C., 2015. Landfast sea ice monitoring using multisensor fusion in the Antarctic. GISci. Remote Sens. 52 (2), 239–256.

Kovacs, K.M., Lydersen, C., Overland, J.E., Moore, S.E., 2011. Impacts of changing sea-ice conditions on Arctic marine mammals. Mar. Biodivers. 41 (1), 181–194.

Kumar, L., Sinha, P., 2014. Mapping salt-marsh land-cover vegetation using high-spatial and hyperspectral satellite data to assist wetland inventory. GISci. Remote Sens. 51 (5), 483–497.

Kunkee, D.B., Poe, G.A., Boucher, D.J., Swadley, S.D., Hong, Y., Wessel, J.E., Uliana, E.A., 2008. Design and evaluation of the first Special Sensor Microwave Imager/Sounder.

IEEE Trans. Geosci. Remote Sens. 46 (4), 863–883.
Lee, S., Han, H., Im, J., Jang, E., Lee, M.I., 2017. Detection of deterministic and probabilistic convection initiation using Himawari-8 Advanced Himawari Imager data. Atmos. Meas. Tech. 10 (5), 1859–1874.
Leigh, S., Wang, Z., Clausi, D.A., 2014. Automated ice–water classification using dual polarization SAR satellite imagery. IEEE Trans. Geosci. Remote Sens. 52 (9), 5529–5539.
Li, M., Im, J., Beier, C., 2013. Machine learning approaches for forest classification and change analysis using multi-temporal Landsat TM images over Huntington Wildlife Forest. GISci. Remote Sens. 50 (4), 361–384.
Lilliefors, H.W., 1967. On the Kolmogorov-Smirnov test for normality with mean and variance unknown. J. Am. Stat. Assoc. 62 (318), 399–402.
Liu, M., Liu, X., Liu, D., Ding, C., Jiang, J., 2015. Multivariable integration method for estimating sea surface salinity in coastal waters from in situ data and remotely sensed data using random forest algorithm. Comput. Geosci. 75, 44–56.
Long, J.A., Lawrence, R.L., Greenwood, M.C., Marshall, L., Miller, P.R., 2013. Object-oriented crop classification using multitemporal ETM+ SLC-off imagery and random forest. GISci. Remote Sens. 50 (4), 418–436.
Lubin, D., Garrity, C., Ramseier, R.O., Whritner, R.H., 1997. Total sea ice concentration retrieval from the SSM/I 85.5 GHz channels during the Arctic summer. Remote Sens. Environ. 62, 63–76.
Mahlstein, I., Knutti, R., 2012. September Arctic sea ice predicted to disappear near 2°C global warming above present. J. Geophys. Res. 117, D06104. http://dx.doi.org/10.1029/2011JD016709.
Mäkynen, M., Hallikainen, M., 2004. Investigation of C-and X-band backscattering signatures of Baltic Sea ice. Int. J. Remote Sens. 25 (11), 2061–2086.
Mäkynen, M., Kern, S., Rösel, A., Pedersen, L.T., 2014. On the estimation of melt pond fraction on the Arctic Sea ice with ENVISAT WSM images. IEEE Trans. Geosci. Remote Sens. 52 (11), 7366–7379.
Markus, T., Cavalieri, D.J., 2000. An enhancement of the NASA Team sea ice algorithm. IEEE Trans. Geosci. Remote Sens. 38 (3), 1387–1398.
Markus, T., Dokken, S.T., 2002. Evaluation of late summer passive microwave Arctic sea ice retrievals. IEEE Trans. Geosci. Remote Sens. 40 (2), 348–356.
Maslanik, J.A., Fowler, C., Stroeve, J., Drobot, S., Zwally, J., Yi, D., Emery, W., 2007. A younger, thinner Arctic ice cover: increased potential for rapid, extensive sea-ice loss. Geophys. Res. Lett. 34, L24501. http://dx.doi.org/10.1029/2007GL032043.
Maslanik, J., Stroeve, J., Fowler, C., Emery, W., 2011. Distribution and trends in Arctic sea ice age through spring 2011. Geophys. Res. Lett. 38, L13502. http://dx.doi.org/10.1029/2011GL047735.
Meier, W.N., 2005. Comparison of passive microwave ice concentration algorithm retrievals with AVHRR imagery in Arctic peripheral seas. IEEE Trans. Geosci. Remote Sens. 43 (6), 1324–1337.
Okuyama, A., Imaoka, K., 2015. Intercalibration of Advanced Microwave Scanning Radiometer-2 (AMSR2) brightness temperature. IEEE Trans. Geosci. Remote Sens. 53 (8), 4568–4577.
Overland, J.E., Wang, M., 2013. When will the summer Arctic be nearly sea ice free? Geophys. Res. Lett. 40, 2097–2101. http://dx.doi.org/10.1002/grl.50316.
Overland, J.E., Wood, K.R., Wang, M., 2011. Warm Arctic—cold continents: climate impacts of the newly open Arctic Sea. Polar Res. 30, 1–14.
Perovich, D.K., Tucker III, W.B., Ligett, K.A., 2002. Aerial observations of the evolution of ice surface conditions during summer. J. Geophys. Res. 107 (C10), 8048. http://dx.doi.org/10.1029/2000JC000449. (2002).
Pirie, W., 2006. Spearman rank correlation coefficient. In: Encyclopedia of Statistical Sciences. John Wiley & Sons, Inc..
Pogson, L., Geldsetzer, T., Buehner, M., Carrieres, T., Ross, M., Scott, K.A., 2017. Collecting empirically derived SAR characteristic values over one year of sea ice environments for use in data assimilation. Mon. Weather Rev. 145 (1), 323–334.
Ressel, R., Frost, A., Lehner, S., 2015. A neural network-based classification for sea ice types on X-band SAR images. IEEE J. Sel. Top. Appl. Earth Observ. Remote Sens. 8 (7), 3672–3680.
Rhee, J., Park, S., Lu, Z., 2014. Relationship between land cover patterns and surface temperature in urban areas. GISci. Remote Sens. 51 (5), 521–536.
Rösel, A., Kaleschke, L., Birnbaum, G., 2012. Melt ponds on Arctic sea ice determined from MODIS satellite data using an artificial neural network. Cryosphere 6, 431–446.
Screen, J.A., Simmonds, I., 2010. The central role of diminishing sea ice in recent Arctic temperature amplification. Nature 464 (7293), 1334–1337. http://dx.doi.org/10.1038/nature09051.
Serreze, M.C., Maslanik, J.A., Scambos, T.A., Fetterer, F., Stroeve, J., Knowles, K., Fowler, C., Drobot, S., Barry, R.G., Haran, T.M., 2003. A record minimum arctic sea ice extent and area in 2002. Geophys. Res. Lett. 30 (1110). http://dx.doi.org/10.1029/2002GL016406.
Serreze, M.C., Barrett, A.P., Stroeve, J., 2012. Recent changes in tropospheric water vapor over the Arctic as assessed from radiosondes and atmospheric reanalyses. J. Geophys. Res. 117, D10104. http://dx.doi.org/10.1029/2011JD017421.
Serreze, M.C., Crawford, A.D., Stroeve, J.C., Barrett, A.P., Woodgate, R.P., 2016. Variability, trends, and predictability of seasonal sea ice retreat and advance in the Chukchi Sea. J. Geophys. Res. Oceans 121, 7308–7325. http://dx.doi.org/10.1002/2016JC011977.
Shin, D.-B., Chiu, L.S., Clemente-Colon, P., 2008. Effects of atmospheric water and surface wind on passive microwave retrievals of sea ice concentration: a simulation study. Int. J. Remote Sens. 29 (19), 5717–5731.
Smith, D.M., 1996. Extraction of winter total sea-ice concentration in the Greenland and Barents Seas from SSM/I data. Int. J. Remote Sens. 17 (13), 2625–2646.
Soh, L.-K., Tsatsoulis, C., 1999. Texture analysis of SAR sea ice imagery using gray level co-occurrence matrices. IEEE Trans. Geosci. Remote Sens. 37 (2), 780–795.
Song, W., Dolan, J.M., Cline, D., Xiong, G., 2015. Learning-based algal bloom event recognition for oceanographic decision support system using remote sensing data. Remote Sens. 7, 13564–13585.
Spreen, G., Kaleschke, L., Heygster, G., 2008. Sea ice remote sensing using AMSR-E 89-GHz channels. J. Geophys. Res. 113, C02S03. http://dx.doi.org/10.1029/2005JC003384.
Steele, M., Ermold, W., 2015. Loitering of the retreating sea ice edge in the Arctic Seas. J. Geophys. Res. 120, 7699–7721. http://dx.doi.org/10.1002/2015JC011182.
Steffen, K., Schweiger, A., 1991. NASA team algorithm for sea ice concentration retrieval from Defense Meteorological Satellite Program special sensor microwave imager: comparison with Landsat satellite imagery. J. Geophys. Res. 96 (C12), 21971–21987. http://dx.doi.org/10.1029/91JC02334.
Stroeve, J.C., Serreze, M.C., Holland, M.M., Kay, J.E., Malanik, J., Barrett, A.P., 2012. The Arctic's rapidly shrinking sea ice cover: a research synthesis. Clim. Chang. 110, 1005–1027.
Stroeve, J.C., Markus, T., Boisvert, L., Miller, J., Barrett, A., 2014. Changes in Arctic melt season and implications for sea ice loss. Geophys. Res. Lett. 41, 1216–1225. http://dx.doi.org/10.1002/2013GL058951.
Stroeve, J.C., Jenouvrier, S., Campbell, G.G., Barbraud, C., Delord, K., 2016. Mapping and assessing variability in the Antarctic marginal ice zone, pack ice and coastal polynyas in two sea ice algorithms with implications on breeding success of snow petrels. Cryosphere 10, 1823–1843.
Swart, N.C., Fyfe, J.C., Hawkins, E., Kay, J.E., Jahn, A., 2015. Influence of internal variability on Arctic sea-ice trends. Nat. Clim. Chang. 5, 86–89. http://dx.doi.org/10.1038/nclimate2483.
Tonboe, R.T., Eastwood, S., Lavergne, T., Sørensen, A.M., Rathmann, N., Dybkjær, G., Pedersen, L.T., Høyer, J.L., Kern, S., 2016. The EUMETSAT sea ice concentration climate data record. Cryosphere 10, 2275–2290.
Torbick, N., Corbiere, M., 2015. Mapping urban sprawl and impervious surfaces in the northeast United States for the past four decades. GISci. Remote Sens. 52 (6), 746–764.
Vihma, T., 2014. Effects of Arctic sea ice decline on weather and climate: a review. Surv. Geophys. 35, 1175–1214.
Vinnikov, K.Y., Robock, A., Stouffer, R.J., Walsh, J.E., Parkinson, C.L., Cavalieri, D.J., Mitchell, J.F.B., Garrett, D., Zakharov, V.F., 1999. Global warming and Northern Hemisphere sea ice extent. Science 286 (5446), 1934–1937. http://dx.doi.org/10.1126/science.286.5446.1934.
Wilcoxon, F., 1945. Individual comparisons by ranking methods. Biom. Bull. 1 (6), 80–83.
Woodgate, R.A., Weingartner, T., Lindsay, R., 2010. The 2007 Bering Strait oceanic heat flux and anomalous Arctic sea-ice retreat. Geophys. Res. Lett. 37, L01602. http://dx.doi.org/10.1029/2009GL041621.
Zakhvatkina, N.Y., Alexandrov, V.Y., Johannessen, O.M., Sandven, S., Frolov, I.Y., 2013. Classification of sea ice types in ENVISAT synthetic aperture radar images. IEEE Trans. Geosci. Remote Sens. 51 (5), 2587–2600.
Zhang, J., Lindsay, R., Steele, M., Schweiger, A., 2008. What drove the dramatic retreat of arctic sea ice during summer 2007? Geophys. Res. Lett. 35, L11505. http://dx.doi.org/10.1029/2008GL034005.
Zhao, X., Su, H., Stein, A., Pang, X., 2015. Comparison between AMSR-E ASI sea-ice concentration product, MODIS and pseudo-ship observations of the Antarctic sea-ice edge. Ann. Glaciol. 56 (69), 45–52.